Improvements to the Assimilation of Doppler Radial Winds for Convection-Permitting Forecasts of a Heavy Rain Event

DONALD E. LIPPI

IMSG, NOAA/Environmental Modeling Center, and Department of Atmospheric and Oceanic Science,
University of Maryland, College Park, College Park, Maryland

JACOB R. CARLEY

NOAA/Environmental Modeling Center, College Park, Maryland

DARYL T. KLEIST

NOAA/Environmental Modeling Center, and Department of Atmospheric and Oceanic Science,
University of Maryland, College Park, College Park, Maryland

ABSTRACT

This work describes developments to improve the Doppler radial wind data assimilation scheme used in the National Centers for Environmental Prediction (NCEP) Gridpoint Statistical Interpolation (GSI) data assimilation system with a focus on convection-permitting, 0–18-h forecasts of a heavy precipitation single case study. This work focuses on two aspects: 1) the extension of the radial wind observation operator to include vertical velocity and 2) a refinement of the radial wind super-observation processing. The refinement includes reducing the magnitude of observation smoothing and allowing observations from higher scan angles into the analysis with the intent to improve the assimilation of the radar data for operational, convection-permitting models. The results of this study demonstrate that there is sensitivity to the refinement in super-observation settings. The inclusion of vertical velocity in the observation operator is shown to have a neutral to slightly positive impact on the forecast. Results from this study are suggested to be used as a foundation to prioritize future research into the effective assimilation of radial winds in an operational setting.

1. Introduction and background

Only four national centers assimilate Doppler radar radial velocities (i.e., radial winds) in operational, convective-scale systems: Météo-France, the Met Office, the National Oceanic and Atmospheric Administration (NOAA) National Centers for Environmental Prediction (NCEP), and the Japan Meteorological Agency (Gustafsson et al. 2018). NCEP first assimilated radial winds during the 1996 summer Olympics in Atlanta, Georgia; however, it was not until 2006 that radial winds were assimilated operationally in the 12-km North American Mesoscale Forecast System (NAM) (http://www.emc.ncep.noaa.gov/NAM/clog.php). Operational numerical weather prediction (NWP) models have since progressed to convection-permitting resolutions

(i.e., where convection is not parameterized) as a result of increased computer power and scientific advancement. Operational data assimilation systems, on the other hand, have not yet progressed to best leverage radial winds for convective-scale NWP systems. The assimilation of radial winds from the U.S. Weather Surveillance Radar-1988 Doppler network (Crum and Alberty 1993) has received a great deal of focus over the past few decades in the research community since Doppler radar is one of the only networks of instruments capable of sampling the storm-scale environment. Many studies (e.g., Gao et al. 2004; Xiao et al. 2005; Gao and Stensrud 2014; Johnson et al. 2015) have shown methods for assimilating radial winds that can benefit the analysis and forecast of convection-permitting models—most of these configurations are not yet suited for operational application owing to computational expense (e.g., compute time, nodes required, disk space). In this study, the focus

Corresponding author: Donald E. Lippi, donald.e.lippi@noaa.gov

is on the assimilation of the radial wind observations. The exploration of the direct assimilation of radar reflectivity along with radial winds is beyond the scope of this manuscript and is the subject of complementary, collaborative efforts (e.g., Duda et al. 2019). However, reflectivity is used indirectly in all experiments in this study by applying radar-derived latent heating tendencies in the forward part of the digital filter initialization (Rogers et al. 2017; Gustafsson et al. 2018; Peckham et al. 2016).

Radial wind observations (Liu et al. 2016) from scan angles greater than 5° have historically been ignored for assimilation in operations because data coverage reduces rapidly as the elevation angle increase (Fig. 1). Additionally, model horizontal grid spacing was sufficiently coarse that one could ignore the analysis of nonhydrostatic motions when the radial wind assimilation algorithm was originally implemented at NCEP. NCEP's radial wind observation operator did not account for vertical motion which necessitated the restriction of a maximum allowable elevation angle in order to exclude observations with high scan elevation angles from contaminating the analysis, as the contribution from vertical motions would potentially become non-negligible at such angles. Each of the other centers that assimilate radial wind observations also only consider the horizontal wind components in their corresponding observation operator (Lindskog et al. 2004; Simonin et al. 2014; Liu et al. 2005; Ishikawa and Koizumi 2006). By limiting the number of scan elevations (Fig. 1) in the assimilation process, a considerable amount of potentially useful information is discarded. Moreover, ignoring vertical velocity in the vicinity of strongly nonhydrostatic flows [i.e., where vertical velocity can be significant $(5–50\,\mathrm{m\,s^{-1}})$], is potentially problematic. Therefore, the Gridpoint Statistical Interpolation system's (GSI; Wu et al. 2002) radial wind observation operator is extended to include vertical velocity. In future related studies, the inclusion of vertical velocity in the assimilation system will have potentially important implications for storm-scale models by helping to establish some of the nonhydrostatic dynamics associated with deep convective storms, thus leading to an improved forecast of these storms. However, due to current limitations of the model used in this study, the analysis of vertical velocity does not directly feed back into the forecast but acts primarily as a sink term in the observation operator. This allows the analysis of vertical velocity to have an indirect impact on the resulting forecast which has been shown through testing.

Another aspect to consider for improving the radial wind assimilation is reducing the errors that arise from the disparity between observation and model resolution (i.e., errors of representativeness) (Janjić et al. 2018). Prior to assimilation, the radial wind observations
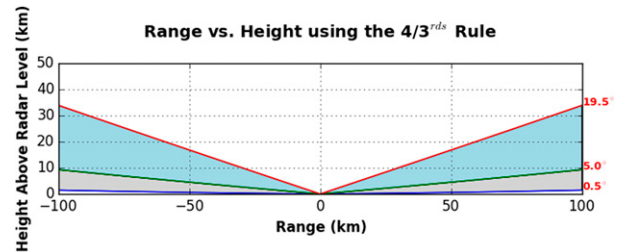

FIG. 1. Radar beam height estimation in km above radar level as a function of range and elevation angle using the 4/3rds rule for standard atmospheric refraction. The gray shaded area shows the elevation angles assimilated prior to this work with the maximum elevation angle restricted to 5°. The blue shaded area corresponds to the max elevation angle of WSR-88Ds from the available volume coverage patterns and can be considered the volume that could potentially be assimilated when accounting for vertical velocity in the observation operator.

are on local polar radar coordinates having dimensions approximately 1° azimuth × 250-m gates with a temporal frequency of 5–10 min. The spatial and temporal resolution of this data exceeds the resolution of most operational analysis systems (e.g., a 9-km analysis grid). To account for some degree of representativeness error, it is standard practice to combine the radial wind observations to create so-called "super-observations" (e.g., Rihan et al. 2008; Lindskog et al. 2004; Simonin et al. 2014; Wheatley et al. 2015). Super-observation methods vary in technique, but all have the same purpose and naturally involve some degree of smoothing of the information content and underlying variance in the observation field. The super-observation technique used in the GSI follows the method of Alpert and Kumar (2007) using tunable parameters that have not been modified in operations since the advent of convection-permitting NWP. The super-observation parameters require revisiting as operational NWP and data assimilation moves toward resolutions where some of these mesoscale convective circulations are resolved. Refining these parameters will help retain storm-scale information content that, historically, would have been necessarily smoothed.

This study investigates the impacts and sensitivity of radial wind assimilation on a convection-permitting forecast system with specific attention to the formulation of the observation operator and super-observation preprocessing. The modifications to the radial wind assimilation scheme in the present study are considered first steps toward advancing the use of these observations at the convective-scale in an operational setting.

In section 2, the model and data assimilation systems are described along with a description of the enhancements to the existing radial wind observation operator.
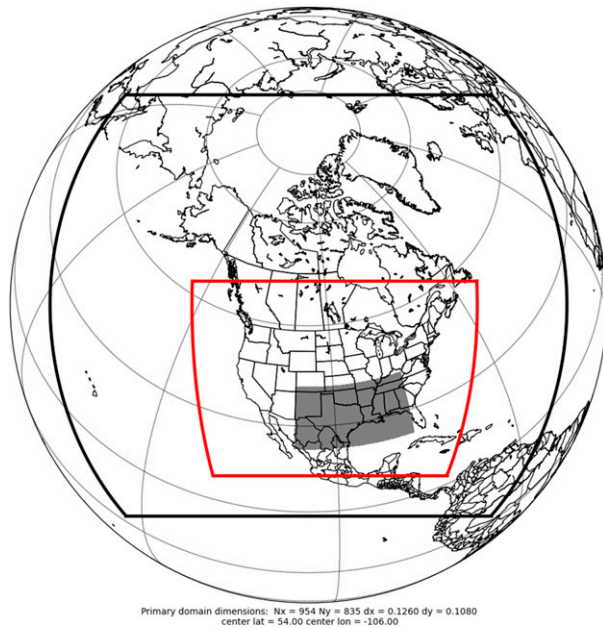
FIG. 2. Computational and verification domains. The outer (black) and inner (red) domains are the 12-km parent and 3-km CONUS nest computational domains, respectively. The objective verification statistics were calculated over the inner (gray shaded) domain located over the south-central (SC) United States using 5-km grid spacing.

The results are presented in section 3. This work is concluded in section 4 with a summary and a discussion of future work.

2. Methods

a. Model and data assimilation configuration

Retrospective forecasts were produced using the North American Mesoscale Forecast System, version 4 (NAMv4; Rogers et al. 2017). The NAMv4 runs hourly data assimilation cycles and was reconfigured to issue 36-h forecast four times per day at 0000, 0600, 1200, and 1800 UTC over the 12-km parent and 3-km CONUS (Fig. 2) domains and 18-h forecasts at each intermediate hour (e.g., 0100, 0200, 0300, 0400, and 0500 UTC

etc.) over the 3-km CONUS nest. Gustafsson et al. (2018) and Djalalova et al. (2016) provide additional information about the data assimilation cycling and other model characteristics of the NAMv4 CONUS nest forecast system. The review paper Gustafsson et al. (2018) also provides configurations for other operational centers supporting convective-scale data assimilation and NWP. The configurations used by the parent and CONUS nest domains are summarized in Table 1.

Data assimilation is performed using the GSI (Wu et al. 2002) system. The GSI is a variational analysis system formulated in model grid space and is used in many operational applications at NCEP, such as the NAMv4 forecast system (Rogers et al. 2017), the Global Forecast System (Kleist et al. 2009), the Rapid and High Resolution Rapid Refresh systems (Hu et al. 2017), and the Real-Time Mesoscale Analysis system (De Pondeca et al. 2011). In this study, the GSI is configured using a hybrid three-dimensional ensemble-variational algorithm (3DEnVar; Wang et al. 2013; Lorenc 2013; Kleist and Ide 2015; Wu et al. 2017) where the static covariance is implicitly blended with an ensemble covariance through the extended control variable method (Lorenc 2003; Wang 2010) and uses a T574 (~35-km grid spacing) 80-member ensemble from the Global Forecast System to provide the ensemble background error covariance (Wu et al. 2017). The weighting between the static and the flow-dependent, ensemble background error covariance is set to 25% and 75%, respectively, which is consistent with the settings used in the operational NAMv4's 3-km CONUS nest data assimilation scheme. The univariate portion of the static background error covariance is modeled using recursive filters (Purser et al. 2003a,b) and statistical balances are employed to account for the cross covariances between control variables (e.g., streamfunction with balanced temperature, velocity potential, and surface pressure). In regional applications, recursive filters are also used to impose localization of the alpha control variable as part of the ensemble-based background error covariance (Wu et al. 2017; Purser et al. 2003a,b). The static background error covariance

TABLE 1. Summary of the configuration and physical parameterizations used by the two NMMB domains.

Domain	Grid space	Radiation (LW/SW)	Microphysics	Turbulence	Surface layer	Land surface	Gravity wave drag	Cumulus
Parent	12 km	RRTMG (Mlawer et al. 1997; Iacono et al. 2008)	Ferrier–Aligo (Aligo et al. 2018)	MYJ (Janjić 2001)	MYJ (Janjić 2001)	Noah (Ek et al. 2003)	On (Alpert 2004)	BMJ (Janjić 1994)
CONUSnest	3 km	RRTMG (Mlawer et al. 1997; Iacono et al. 2008)	Ferrier–Aligo (Aligo et al. 2018)	MYJ (Janjić 2001)	MYJ (Janjić 2001)	Noah (Ek et al. 2003)	None	None

statistics were estimated using the so-called NMC method (Parrish and Derber 1992), which averages the differences between lagged forecast pairs (e.g., 24- and 48-h forecasts) valid at the same time. The static background error covariance is identical to that used in the operational NAMv4 system, formulated to be isotropic and vary vertically and latitudinally.

The comparatively coarse nature of the static background error covariance and ensembles leveraged in the hybrid 3DEnVar system limits the finescale nature of the analysis increments that can be prescribed. Therefore, the data assimilation is performed on a grid that is 3 times coarser than the model grid (i.e., a 9-km analysis grid). This practice is consistent with the operational configuration of the NAMv4 3-km CONUS nest system and allows for efficient use of computational resources without changing the characteristics of the analysis; however, this aspect will be revisited in future work when a finescale convection-permitting ensemble is included in the EnVar algorithm.

b. *Extending the radial wind operator for vertical velocity*

Data assimilation requires the comparison of model state variables to observations. As is the case for many observation types, radial wind is not a direct model prognostic variable; therefore, a relationship which transforms the model state $\mathbf{x}$ into an observation equivalent $\mathbf{y}$ must be used. This transformation occurs with the use of the observation operator H. The general relationship between the model state variables and observations can be written as follows:

$$\mathbf{y} = H(\mathbf{x}) + \varepsilon^o, \tag{1}$$

where ε^o is the observational error. Errors associated with radial wind observations can be attributed to four main sources: instrument error, preprocessing errors, errors of representativeness, and errors introduced by the observation operator (Waller et al. 2016). Errors introduced by the observation operator are the result of omissions and approximations of the equation.

1) THE RADIAL WIND OBSERVATION OPERATOR

The original GSI radial wind operator took the following form:

$$\mathbf{V}_r(\theta, \alpha) = u\cos(\theta)\cos(\alpha) + v\sin(\theta)\cos(\alpha), \tag{2}$$

where $\mathbf{V}_r$ is the radial wind observation, u and v are the model horizontal wind components, θ is 90° minus the azimuth angle of the radar, and α is the elevation (or tilt) angle of the radar. The formulation here uses the azimuthal directions based on the unit circle rather

than the cardinal directions. The effects of Earth's curvature and atmospheric refraction are accounted for via the four-thirds approximation (e.g., Ge et al. 2010). Wind rotation is also included to accommodate relevant coordinate conversions. These corrections are included in the azimuth and elevation angles of Eq. (2).

Historically, the radial wind operator has not accounted for the influence of vertical motion, owing to the hydrostatic scales of motion to which it was applied (e.g., 12 km). Due to this restriction, radial wind observations associated with scan elevation angles greater than 5° were routinely discarded in order to reduce the impact of vertical motion on the radial wind field. Using the simplified observation operator [Eq. (1)] will produce a bias error in the model equivalent value when high elevation angles (e.g., Fig. 1) are used considering the vertical component of the wind could make a nontrivial contribution in the observed radial wind especially in the presence of strongly nonhydrostatic motions. However, the sensitivity to this assumption will be a function of several factors such as the model resolution.

To extend the radial wind observation operator to include the vertical component of the wind, Eq. (2) was modified to include a third term:

$$V_r(\theta, \alpha) = u\cos(\theta)\cos(\alpha) + v\sin(\theta)\cos(\alpha) + w\sin(\alpha), \tag{3}$$

where w represents vertical velocity.

The difference between these two observation operators is shown in Fig. 3. When w is zero, there is no difference between the observation operators. When w is positive (negative), Eq. (2) underestimates (overestimates) the radial wind. The magnitude of error is strongly dependent on the vertical velocity as well as the elevation angle. The maximum possible error for an elevation angle more practically used in an operational scenario, less than 20°, with an assumed vertical velocity of $10\,\mathrm{m\,s^{-1}}$, is $\pm 3\,\mathrm{m\,s^{-1}}$. Such large vertical motions are not unusual for deep convection. This error would be much greater (less) in regions of very strong (weak) vertical motion and/or steeper (less steep) elevation angles.

Large raindrops, around 5 mm in diameter, have terminal velocities (w_t) of about $10\,\mathrm{m\,s^{-1}}$ (Spilhaus 1948) leading to an error from Eq. (3) of $w_t\sin(\alpha)$, or about $1.7\,\mathrm{m\,s^{-1}}$ in the most extreme cases for elevation angles of 10°—the highest elevation angle considered in the experiments. Equation (3) more accurately simulates the radial winds as compared to Eq. (2), although still contains simplifications that should be considered in the future (e.g., hydrometeor terminal velocity and

Doppler Radial Wind Observation Operator Differences
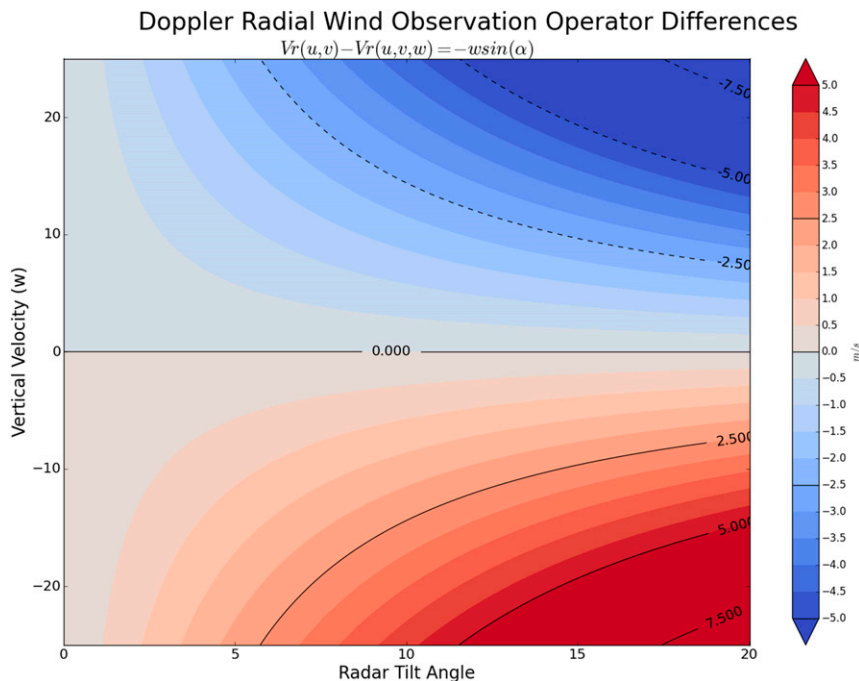$$Vr(u,v) - Vr(u,v,w) = -w\sin(\alpha)$$

FIG. 3. The difference [Eqs. (2) and (3)] between the original observation operator [Eq. (2)] and the observation operator with a term for vertical velocity [Eq. (3)].

beam broadening; Fabry 2010). Nonetheless, this change results in a more physically consistent forward model, reduces representativeness error, and allows for relaxing the maximum radar elevation angle to beyond 5°, ultimately allowing a larger volume of observations to be assimilated.

2) VERTICAL VELOCITY ANALYSIS CONTROL VARIABLE

The variational analysis (e.g., Hybrid 3DEnVar) is determined based on the minimization of a cost function. The cost function is measured, in part, by the combination of the departures of the observations and background from a select set of analysis control variables. The control variables may be any set of model or model-related variables. In the case of the GSI, the control variables are chosen with considerations toward Gaussianity and multivariate balance. For example, the control variables for the NAMv4 CONUS nest applications are streamfunction, unbalanced velocity potential, unbalanced temperature, unbalanced surface pressure, and normalized specific humidity. During the minimization of the cost function, increments to the control variables are made and then added to the initial background forecast. Only increments to variables related to the control variables (directly or indirectly through multivariate relationships) can be affected in the resulting analysis. Vertical velocity was added

as a control variable to support the analysis of non-hydrostatic motion, which follows from the work above to improve the radial wind observation operator.

The experiments here utilize an 80-member ensemble from the Global Data Assimilation System (GDAS) running at T574 (~35-km). The ensemble-based analysis increment is constructed by utilizing the extended control variable method (Lorenc 2003) used in the GSI hybrid 3DEnVar cost function (Wu et al. 2017). The ensemble perturbation wind variables are u and v and are not converted into balanced and unbalanced parts. Ensemble perturbations of w are not used at this time, owing to the fact that the perturbations are from a global, hydrostatic ensemble.

The model used in this study, the Nonhydrostatic Multiscale Model on the B-grid (NMMB; Janjić and Gall 2012), *diagnoses* vertical velocity via the non-hydrostatic continuity equation with the knowledge of the hydrostatic and nonhydrostatic pressures and temperature. Therefore, while the model is fully non-hydrostatic, it does not feature a prognostic term specifically for vertical velocity (Janjić and Gall 2012). This presents some difficulty in terms of providing an analyzed vertical motion field to the model; therefore, the associated analysis of vertical velocity in this study serves primarily to reduce error present in the observation operator and therefore improve representativeness. However, limited testing has shown that

the analysis of vertical velocity can indirectly impact the forecast.

3) SINGLE OBSERVATION TESTS

A useful tool for diagnosing several aspects of a data assimilation system is the single observation test. Here, we seek to verify the successful implementation of the radial wind operator using synthetic radial wind observations using a 3DVar configured GSI.[1] Two single observation tests were used to isolate and test the vertical and horizontal components of the observation operator by assigning the elevation angle to two extremes: 90° and 0°, respectively. A 90° elevation angle corresponds to the radar looking straight up, and the 0° elevation angle corresponds to the radar looking tangentially to Earth's surface at the observation location. For the 90° elevation test, the observation was placed about 1 km above ground (corresponding to approximately model level 18; between 800 and 900 hPa) directly over the Fort Hood, Texas, radar (KGRK). The observation for the 0° elevation test was placed about 20 km directly to the east of KGRK about 200 m above ground level (approximately model level 4; between 1000 and 900 hPa). Although it is not geometrically possible for a radial wind observation with an altitude above ground level to have a corresponding 0° elevation angle, synthetic observations are used to facilitate testing by relaxing such rule. This also applies to the 90° test since elevation angles in the real world do not exceed 20° for WSR-88Ds.

An azimuth angle must be defined for the 0° elevation test. The assignment of the azimuth angle will not affect the results of the 90° elevation test since only the vertical term in Eq. (3) will remain. For demonstration purposes, we would like to achieve a positive increment in only the zonal direction for the 0° elevation test (and vertical direction for the 90° elevation test); therefore a 0° azimuth, or eastward pointing radar was chosen. To obtain a positive analysis increment with an eastward (upward) pointing radar, a positive innovation is needed. This is because the innovations are calculated in observation space, and outbound radial winds are positive, which is a westerly (upward) wind for the 0° (90°) elevation test. For both single observation tests, each observation was assigned an innovation of $+1.0 \, \mathrm{m \, s^{-1}}$ with an observation error of $1.0 \, \mathrm{m \, s^{-1}}$. The statistical balance relationships associated with the static background

error covariance were also set to zero to avoid multivariate increments to isolate the impact from the single observation tests (e.g., increments in temperature when only a *u* observation was given). Finally, the assigned winds were assumed Earth relative, and thus the winds were not rotated from latitude–longitude coordinates. This ensures the observation is exactly as prescribed.

From these single observation tests, one can verify that the newly implemented observation operator correctly maps the model state into an observed equivalent quantity so that an analysis increment can be made to the correct wind component according to the given observation specifications (e.g., elevation and azimuth angles). A comparison of the two experiments confirms the successful implementation of the radial wind operator. As expected, the 90° elevation test shows an analysis increment for only vertical velocity (Fig. 4b) depicting an isotropic analysis increment, as expected in a 3DVar analysis. This test used a globally constant value for the vertical velocity background error covariance with a value of $0.7 \, \mathrm{m^2 \, s^{-2}}$ and a horizontal and vertical scale of influence of 27 km and 10 grid units, respectively. In contrast, the 0° elevation test has isotropic increments only in the zonal wind component (Fig. 5a). The length scales for the horizontal wind components, originating from the operational NAMv4 forecast system, are much larger than for vertical velocity hence the comparatively broad increments.

The background error covariance statistics were not recalculated to include vertical velocity for this study since the vertical motion field is a diagnostic quantity in the forecast mode,[2] and therefore acts primarily as a sink term. The specifications used for the background error covariance in the single observation tests are used in the main set of experiments presented in this study. Some sensitivity experiments were also done with alternate length scales and those results will be discussed briefly as well.

c. Creating super-observations of radial wind data

Prior to assimilation, the radial wind observations (Liu et al. 2016) undergo an aggregation and smoothing procedure to generate super-observations. The super-observation technique is employed to remove representativeness errors and reduce the volume of observations,

---

[1] Synthetic observations may refer to observations that cannot be physically possible but are useful in testing the functionality of the data assimilation system.

[2] Recall that the model in this study diagnoses vertical velocity via the nonhydrostatic continuity equation using hydrostatic and nonhydrostatic pressures and temperature. It does not feature a prognostic term for vertical velocity, instead the associated nonhydrostatic prognostic term is nonhydrostatic pressure.
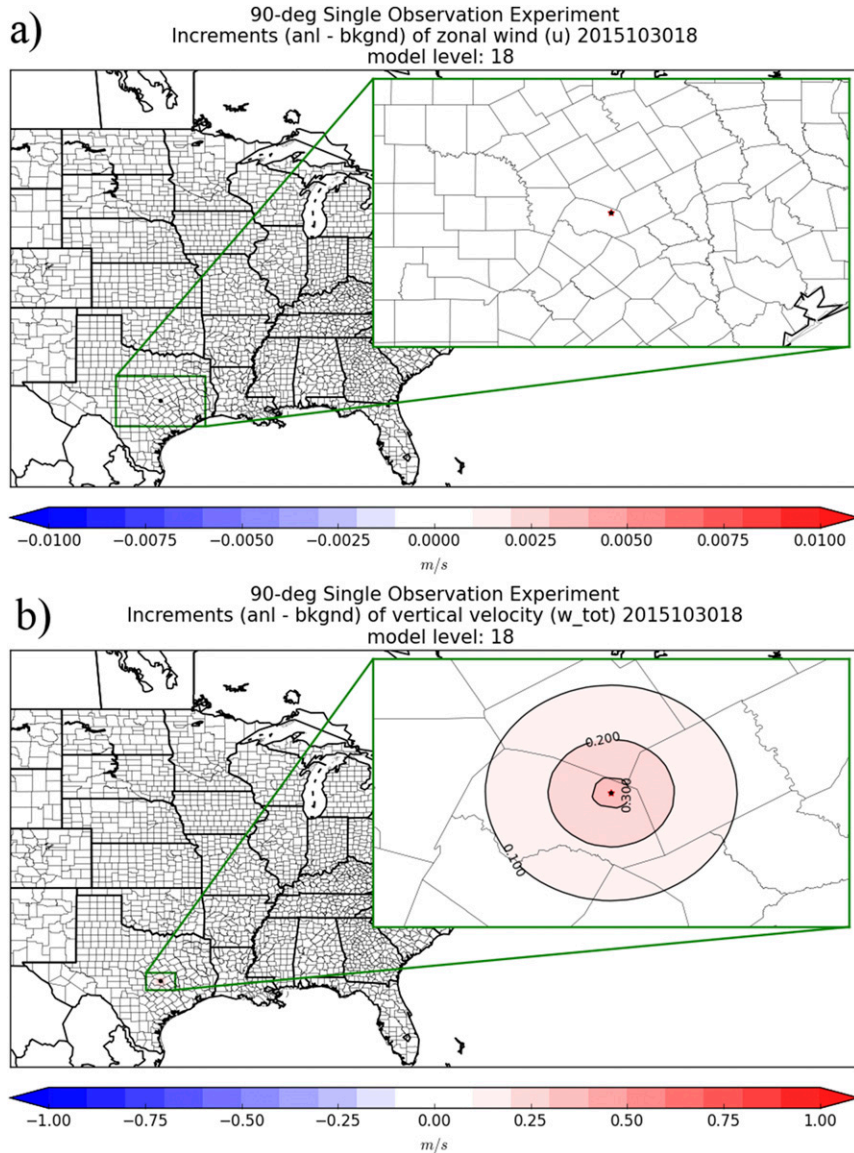
FIG. 4. Results from the 90° tilt single observation test (SOT). The pseudo-observation (black dot) was placed 1 km above the Fort Hood, TX, radar KGRK (red star) with an innovation of $+1\,\mathrm{m\,s^{-1}}$ and an observation error of $1\,\mathrm{m\,s^{-1}}$. 3DVar analysis increments are shown for (a) zonal wind u and (b) vertical velocity w.

which are often redundant and come at the price of additional computational expense (Alpert and Kumar 2007). The super-observation procedure involves a spatial and temporal averaging of the radial wind observations within a volume defined in radar coordinates via the parameters noted in Table 2.

There are seven super-observation parameters: del azimuth, $\Delta\theta$; del elevation angle, $\Delta\varepsilon$; del range, Δr; del time, Δt; maximum elevation angle, ε_{max}; minimum number, N; and maximum range R_{max}. $\Delta\theta$, $\Delta\varepsilon$, and Δr control the width, height, and length of the super-observation box azimuthally, in elevation, and along

the beam, respectively; Δt is the one-half time window for which to include observations; and N is the minimum number of observations that must exist within the super-observation box defined in space and time in order for a super-observation to be calculated. Finally, ε_{max} and R_{max} are the maximum allowable radar elevation angle and maximum range from the radar (i.e., an observation is discarded if it exceeds either of these values). Together, these parameters define a four-dimensional box in radar observation space and time that forms the bounds for which the observations are processed into super-observations. The effects of
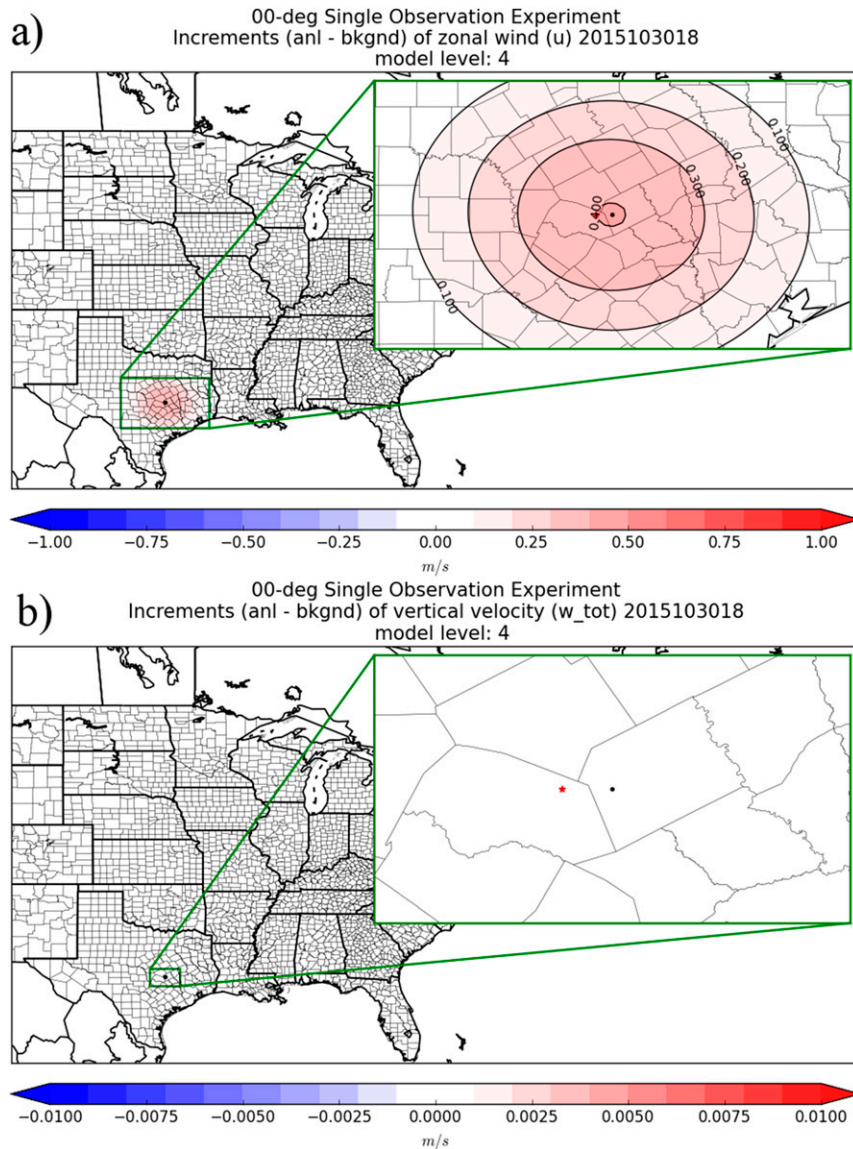
FIG. 5. Results from the 0° tilt single observation test (SOT). The observation (black dot) was placed 20 km directly to the east of the Fort Hood, TX, radar KGRK (red star) about 200 m above ground level with an innovation of $+1\,\mathrm{m\,s}^{-1}$ and an observation error of $1\,\mathrm{m\,s}^{-1}$. 3DVar analysis increments are shown for (a) zonal wind u and (b) vertical velocity w.

the super-observation parameters can be captured by visualizing the radar observations before (Fig. 6a) and after (Figs. 6c,d) the radial winds have undergone super-observation preprocessing. The corresponding radar reflectivity observations are shown in (Fig. 6b) for reference. Through visual comparison, one can see that Fig. 6d features more detail than Fig. 6c when compared to the unprocessed, raw data depicted in Fig. 6a.

The maximum possible number of super-observations per radar at a single time can be estimated using the following equation:

Maximum possible number of super-observations

$$= \frac{360°}{\Delta\theta} \times \frac{R_{\max}}{\Delta R} \times \frac{\alpha_{\max}}{\Delta\alpha}.$$

For the default super-observation settings, there could be up to 28 800 super-observations per radar and up to 158 400 with the modified experimental values. The actual number of super-observations will generally be much lower because observations will exist in only a fraction of the total radar volume. For example, the super-observation counts that correspond to the

TABLE 2. List of the super-observation parameters and their default and experimental values.

Configuration	Azimuth range (°) $\Delta\theta$	Elevation angle range (°) $\Delta\varepsilon$	Radial range (m) Δr	One-half time range (h) Δt	Max elevation angle (°) ε_{max}	Min No. of samples N
Default	5	0.25	5000	±0.500	5	50
Experimental	3	0.25	3000	±0.125	10	10

KGRK radar for the convective period 1800 UTC 30 October 2015 shown in Fig. 6a are 8000 and 25 000 super-observations for the default and modified super-observation settings, respectively.

In addition to visualizing how modifying the super-observation parameters will change the spatial and temporal geometry of the super-observation box, it is also important to understand how this will affect the
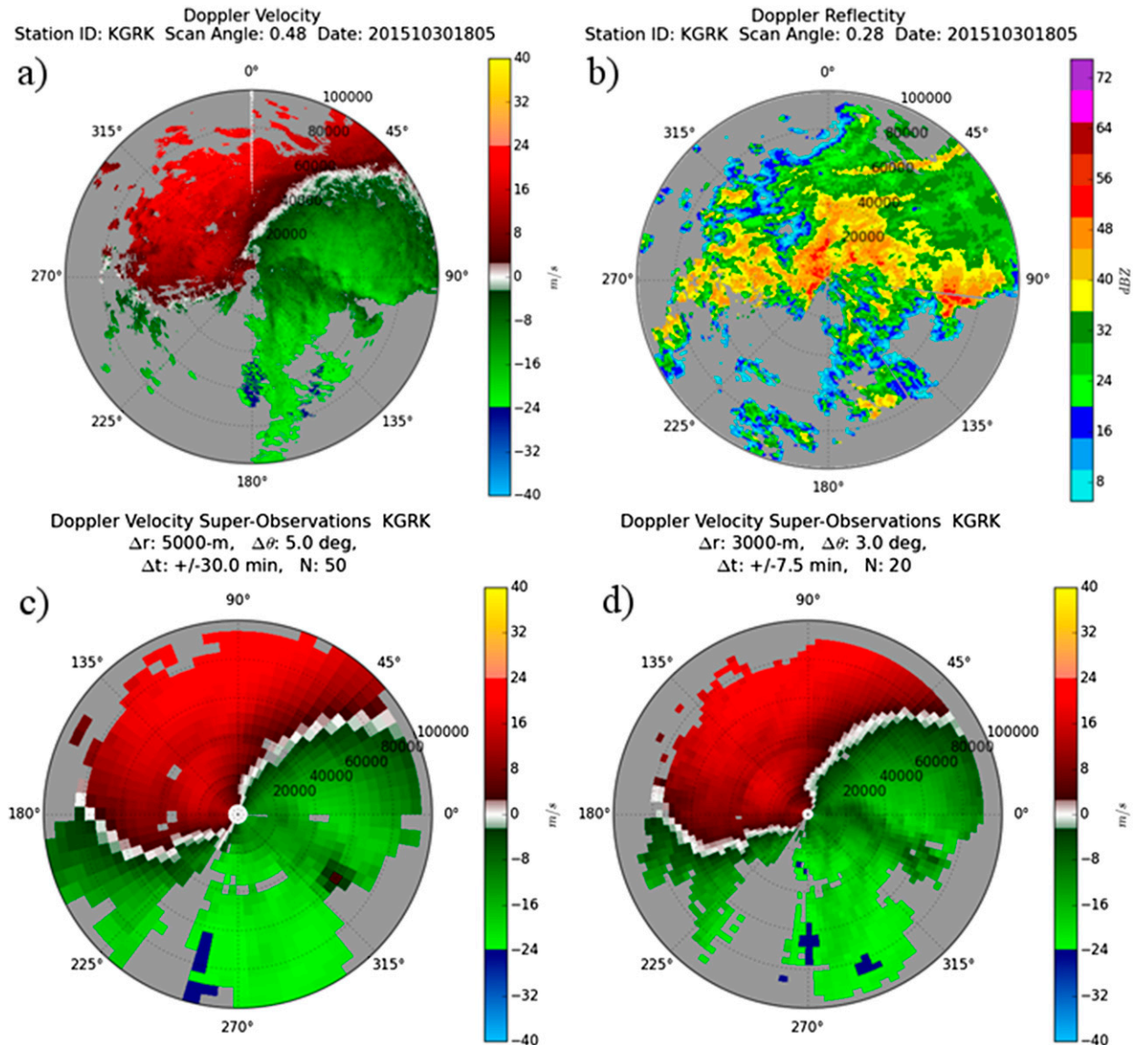

FIG. 6. (a) Level-II radial wind observations before and (c),(d) after super-observation processing using the default super-observation settings and experimental super-observation settings for the radial winds. (b) The associated radar reflectivity for ~1800 UTC 30 Oct 2015 is shown for reference.

processing of the underlying data. A rough estimation of the maximum number of radial wind observations (M_{max}) that can be contained within a single super-observation box can be obtained by

$$M_{max} = \frac{\Delta\theta}{1°} \times \frac{\Delta R}{250\,m} \times 120 \frac{\Delta t}{5\,min}$$

assuming the radial wind observation spatial resolution of $1° \times 250\,m$, a temporal resolution of 5 min, and only one scan per elevation angle. The maximum number of observations per super-observation box can only be estimated due to a few factors:

1) The actual beamwidth may differ slightly from the assumed $1°$. This could increase or decrease the number of observations.
2) During severe weather events, when more aggressive volume coverage patterns may be used, there could be more than one scan at the same tilt. This will increase the number of observations.
3) The $0.25°$ super-observation box height ($\Delta\varepsilon$) may include data from two elevations, possibly increasing the number of observations.
4) When the radar mode changes, scan times may not be 5-min, which could increase or decrease the number of observations.

The estimated number of observations per super-observation box are 1200 and 108 for the specified parameters in Table 2 for the default and modified configurations, respectively.

Figures 7a and 7b depict the distributions of the number of observations per super-observation box for a single time and radar that corresponds with Figs. 6c and 6d, respectively. The default configuration shows a bimodal distribution with a peak near zero and a peak around 650–700 observations but shows that few of the super-observations were generated at or near the maximum possible number of radial winds in a super-observation box (M_{max}). The features represented by radial winds evolve at subhourly intervals which may partially explain the large difference in the actual and estimated number of observations per super-observation box. The default time window for assimilating radial winds is one hour ($\pm30\,min$), but there is no guarantee that those features will exist in or totally encompass a super-observation box during that entire period. For example, a super-observation box may be located near a storm boundary and may include observations from only a few minutes. Observation quality control may also play a role by discarding observations of poor quality.

The large time window for aggregation has the potential to smooth out convective-scale features of interest as they evolve on relatively short time scales. By reducing

the time window of observations to 15 min ($\pm7.5\,min$), the super-observations should be more representative of the analysis time and we see a peak in Fig. 7b at 100–120 observations corresponding to the estimated max number of observations of 108 for the given settings.

d. Experimental design

To test the impact of adding vertical velocity to the radial wind observation operator and the associated sensitivities with super-observation parameters refined to retain more detail, a control simulation and four experiments were initialized at 0000 UTC 30 October 2015 on the 3-km CONUS nest grid (Table 3). The modified super-observation parameter values were chosen based on limited, preliminary testing that showed improved wind analyses balanced with considerations toward the data assimilation system memory limitations.[3]

1) control: Configured to match the operational NAMv4 with the exception of refined radial wind quality control discussed in Lippi et al. (2016) which eliminated the quality check against velocity–azimuth display (VAD) winds. The VAD winds are radar-specific wind profiles derived from the radial wind field and are based on a linearized wind model (Holleman et al. 2005). The procedure of the VAD quality control is to compare the radial wind super-observations to the VAD derived winds. Only observations that agree with the VAD winds within a predetermined tolerance are accepted. This has the impact of retaining only those winds that align with the larger-scale flow derived from the VAD wind profile and discards the winds representative of the convective scale. Since this study focuses on the assimilation of radial wind observations associated with a convective system the VAD quality control step was removed in this work (Lippi et al. 2016).
2) w_incl: As in control, but includes w in the observation operator and as an analysis variable.
3) w_so_elev5: As in w_incl, but uses refined super-observation (so) parameters to retain more detail and keeps the maximum elevation angle at $5°$ (elev5).
4) w_so_elev10: As in w_so_elev5, but raises the maximum elevation angle to $10°$ (elev10).
5) so_elev10: As in w_so_elev10, but w is not used in the observation operator.

---

[3] There are specific run time and disk space limitations that must be considered for implementing a system in operations. In this example we must exercise caution assimilating raw, unprocessed observations which can exceed the available memory on compute nodes. Thinning observations and creating super-observations helps eliminate this issue while also addressing other scientific concerns, such as representativeness.
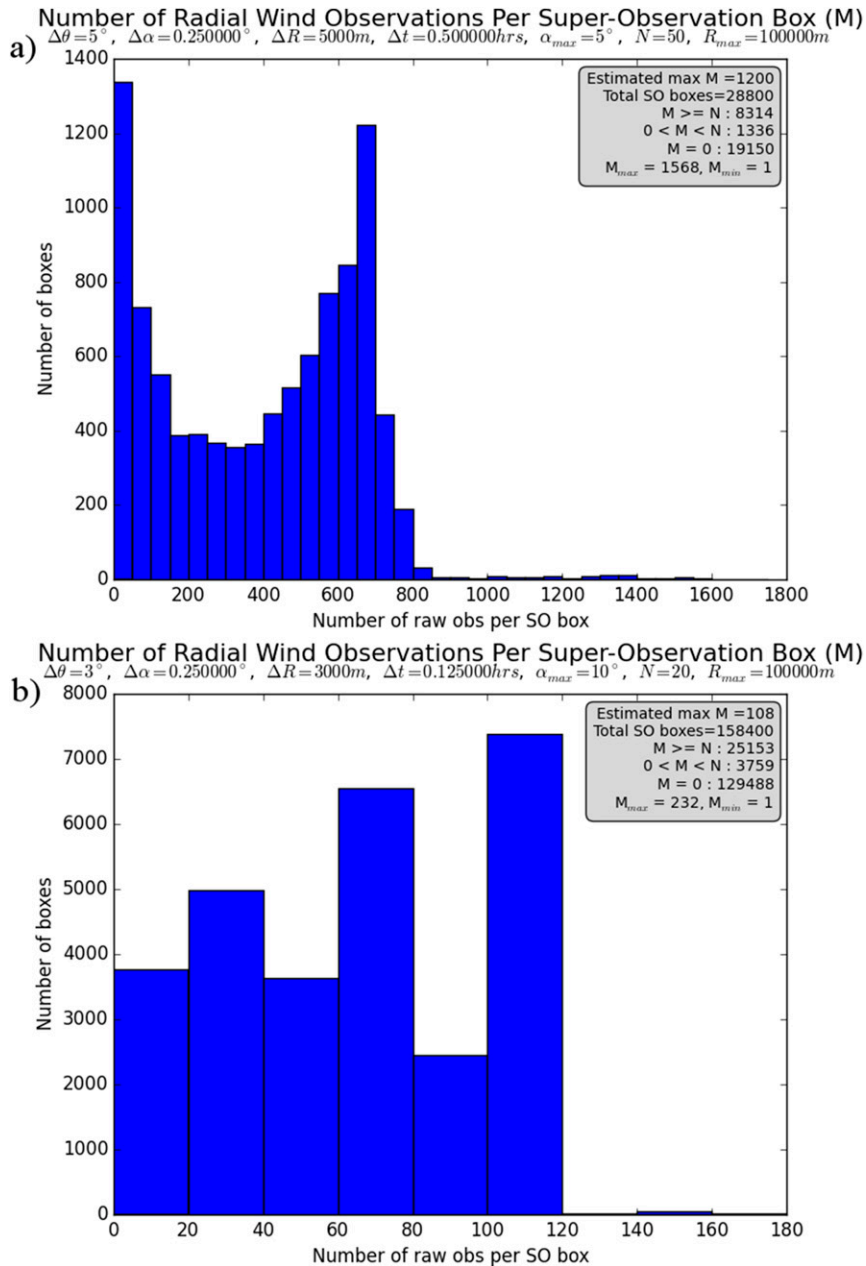
Number of Radial Wind Observations Per Super-Observation Box (M)

a) $\Delta\theta=5°$, $\Delta\alpha=0.250000°$, $\Delta R=5000m$, $\Delta t=0.500000hrs$, $\alpha_{max}=5°$, $N=50$, $R_{max}=100000m$

Estimated max M =1200
Total SO boxes=28800
M >= N : 8314
0 < M < N : 1336
M = 0 : 19150
M_{max} = 1568, M_{min} = 1

Number of Radial Wind Observations Per Super-Observation Box (M)

b) $\Delta\theta=3°$, $\Delta\alpha=0.250000°$, $\Delta R=3000m$, $\Delta t=0.125000hrs$, $\alpha_{max}=10°$, $N=20$, $R_{max}=100000m$

Estimated max M =108
Total SO boxes=158400
M >= N : 25153
0 < M < N : 3759
M = 0 : 129488
M_{max} = 232, M_{min} = 1

FIG. 7. (a),(b) Distribution of the number of radial wind observation per super-observation box (M) for a single time and radar that corresponds with Figs. 6c and 6d, respectively. Additional information appears in the annotation box, which includes the estimated maximum value for M, the total number of super-observations boxes for one radar, the number of super-observation that would be assimilated ($M \geq N$), the count of super-observations that do not meet the requirement of N but have at least one Level-II observation, the count of super-observation boxes with 0 radial wind observations, and finally the maximum and minimum values for M for this case.

e. Verification

Frequency bias (FBIAS) and the fractions skill score (FSS) were used to objectively evaluate forecasts of accumulated precipitation. The verification was computed on a common, 5-km grid that encompassed the area of focus for the case study (Fig. 2; gray shaded). A description for each of the statistical methods follows.

TABLE 3. List of NAMv4 radial wind data assimilation experiments and the configurations for the super-observation settings as well as if vertical velocity is used in the observation operator and as a control variable. Each super-observation parameter ($\Delta\theta$, $\Delta\varepsilon$, Δr, Δt, $\varepsilon_{max,}$ and N) has a distinct impact on the resulting super-observation box size in time and space. $\Delta\theta$, $\Delta\varepsilon$, and Δr control the width, height, and length of the super-observation box azimuthally, in elevation, and along the beam, respectively. Δt is the time window for which to include observations, and N is the minimum number of observations that must exist within the super-observation box defined in space and time in order for a super-observation to be calculated. Finally, ε_{max} is the maximum allowable radar elevation angle (i.e., an observation is discarded if it exceeds this value).

Exp	w	Azimuth range (°) $\Delta\theta$	Elevation angle range (°) $\Delta\varepsilon$	Radial range (m) Δr	One-half time range (h) Δt	Min No. of samples N	Max elevation angle (°) ε_{max}
control	No	5	0.25	5000	±0.500	50	5
w_incl	Yes	5	0.25	5000	±0.500	50	5
w_so_elev5	Yes	3	0.25	3000	±0.125	20	5
w_so_elev10	Yes	3	0.25	3000	±0.125	20	10
so_elev10	No	3	0.25	3000	±0.125	20	10

FBIAS is used to determine if the forecast is too "dry" or too "wet" and is calculated in the following manner:

$$\text{FBIAS} = \frac{\text{hits} + \text{false alarms}}{\text{hits} + \text{misses}}. \qquad (4)$$

Stated more simply, FBIAS is the ratio of "yes" forecasts to "yes" observations.

FBIAS greater than 1 (less than 1) indicates fewer (more) points predicting a given threshold compared to observations [i.e., a dry bias (wet bias)].

The FSS is a neighborhood verification approach which relaxes the requirement for forecast and observed events to match exactly at the grid scale. Instead, the fractional coverage of predicted and observed gridpoint events above a specified threshold is compared over a range of increasing spatial windows (Roberts and Lean 2008).

The FSS is computed in the following manner:

$$\text{FSS} = 1 - \frac{\frac{1}{N}\sum_N (P_f - P_o)^2}{\frac{1}{N}\sum_N P_f^2 + \sum_N P_o^2} = 1 - \frac{\text{FBS}}{\text{FBS}_{\text{worst}}}, \qquad (5)$$

where N is the number of grid points contained within the neighborhood area; P_f is the fractional coverage of forecast events that exceed a predetermined threshold; and P_o is the fractional coverage of observed events that exceed the threshold. The FSS is thus the ratio between the fractional Brier score (FBS; related to the difference between the fractional coverage of predicted and observed events that exceed the threshold) and the worst possible FBS (FBS$_{\text{worst}}$; related to the summation of the total number of forecast and observed fractions that exceed the threshold). FSS reveals how well the forecast resembles the observations at a given spatial window. The FSS ranges from 0 to 1 where 0 would be a complete mismatch and 1 would be a perfect match of forecast events to observed events.

All statistics were aggregated in 3-hourly periods for accumulated precipitation out to 18 h for the 0900, 1200, 1500, and 1800 forecast cycles on 30 October 2015; the 3-hourly cycles are used to accommodate the 3-h buckets of the precipitation observations. A bootstrapping technique, using 2000 replications, was used to test for statistical significance at the 90% confidence level.

f. Case study overview

Retrospective forecasts during the convectively active period of 30–31 October 2015 in the southern plains were made to evaluate the impact of the modifications to the radial wind observation operator as well as the modifications to the super-observation parameters. This case was chosen because it consists of a fairly diverse set of forcing mechanisms including an upper-level short-wave trough, cold front, interaction between the low-level jet (LLJ) and a warm front, and a prefrontal confluence zone. Additionally, this case exhibited heavy precipitation, flooding, damaging winds, and several tornadoes. More than one foot of rain fell in less than 24 h between Austin and San Antonio, Texas (Fig. 8), which caused extensive flooding throughout that region. Another line of heavy precipitation occurred later in the period near Houston, Texas. Several tornadoes rated between EF-0 and EF-2 were reported in these two regions (Fig. 9).

3. Results

a. Data assimilation system fit-to-observations

The analysis impact of the modified observation operator and refined super-observation processing can be diagnosed by comparing the observation-minus-background (OmB) and observation-minus-analysis (OmA) residuals

Obs 24-hr Total Precipitation
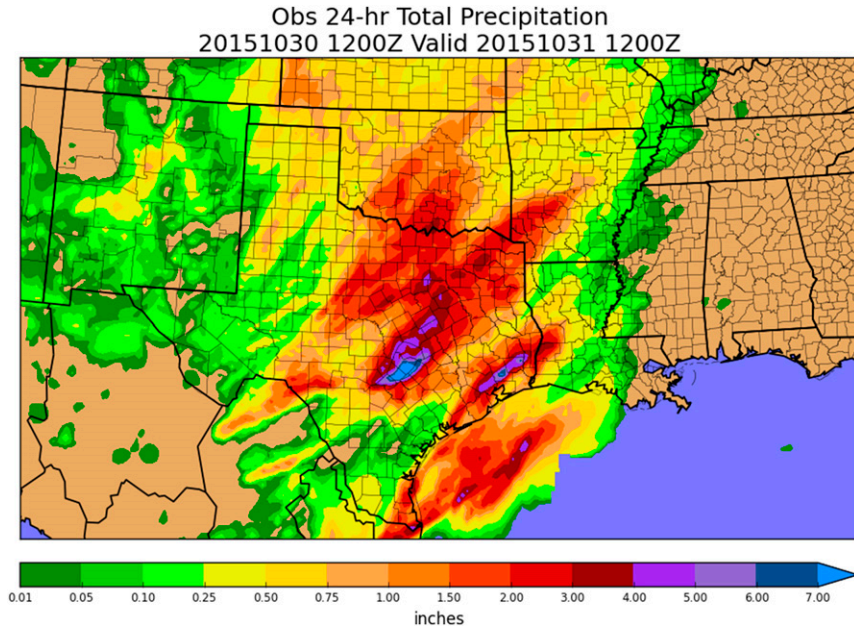### 20151030 1200Z Valid 20151031 1200Z

FIG. 8. NCEP stage IV observed total 24-h precipitation (in.) valid at 1200 UTC 31 Oct 2015
(Lin and Mitchell 2005).

between experiments. Three statistics from the fit-to-observations will be analyzed: observation counts, root-mean-square (RMS) innovation, and bias.

There are two factors that affect the observation counts: event-specific observation availability and experimental-specific factors, which includes the pre-processing of the observations via tunable super-observation parameters. The increase in observation counts from 0900 UTC (Fig. 10a) through 1800 UTC (Fig. 10d) is the result of storms developing within the
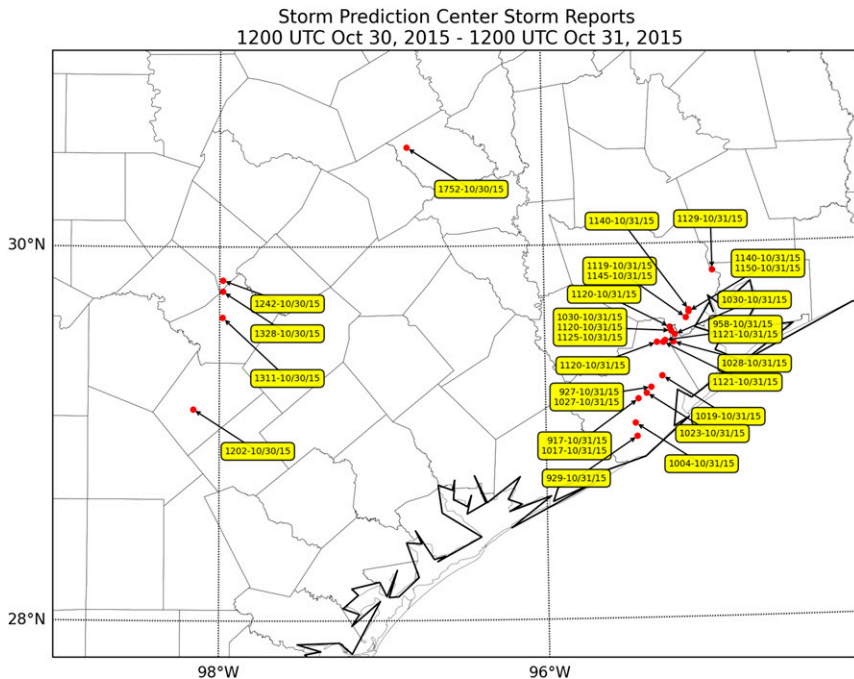

FIG. 9. Tornado reports for 1200 UTC 30 Oct–1200 UTC 31 Oct 2015 from the Storm Prediction Center from the Austin and Houston, TX, areas. All times are in UTC. (Data available online at http://www.spc.noaa.gov/exper/archive/event.php?date=20151030.)
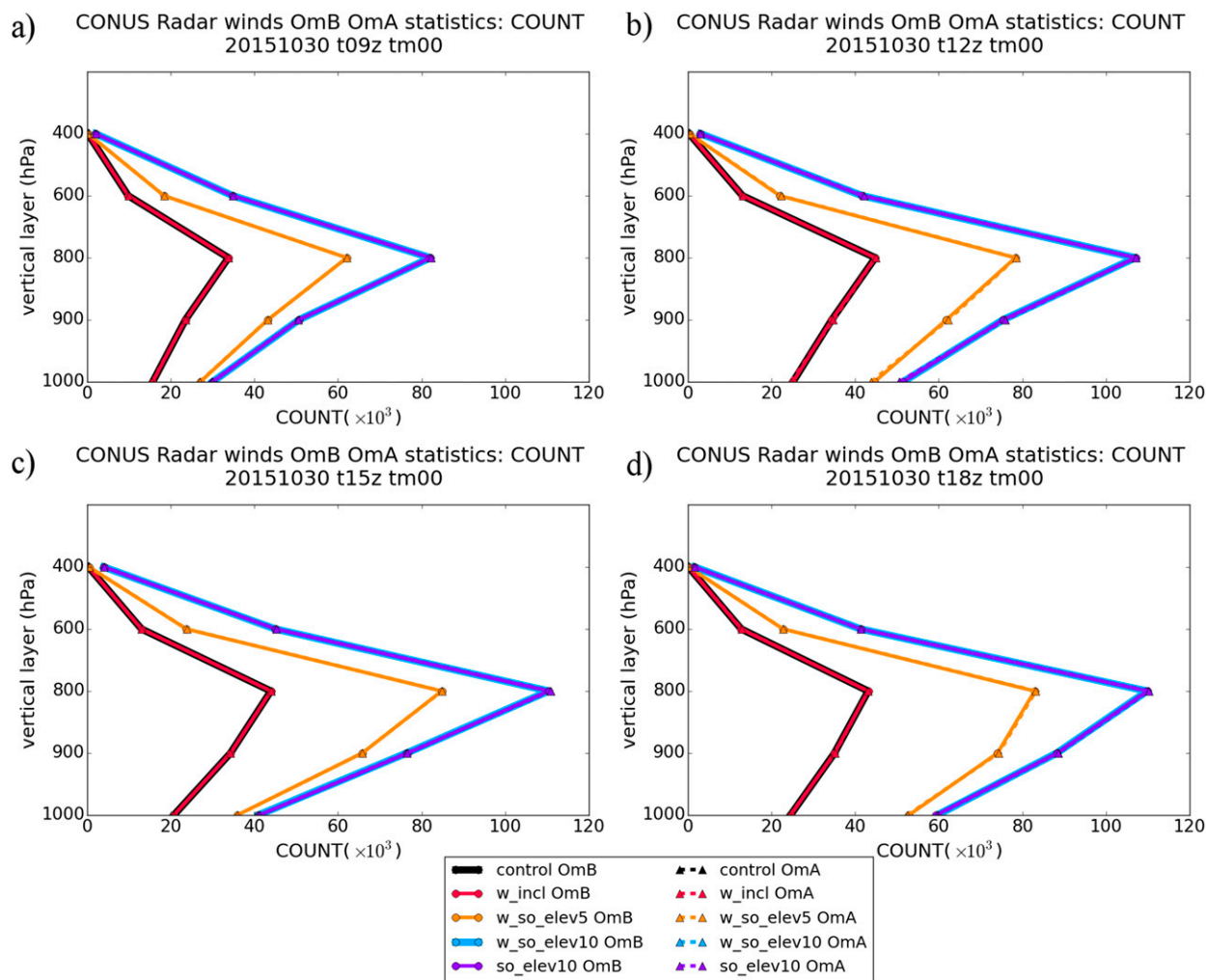
FIG. 10. Counts from the observation minus background (OmB; circles/solid line) and observation minus analysis (OmA; triangles/dashed lines) statistics files over entire CONUS nest domain for the forecast cycles (a) 0900, (b) 1200, (c) 1500, and (d) 1800 UTC 30 Oct 2015. The individual circle/triangle markers along the x axis denote the aggregate values for the total CONUS atmosphere. Note: the OmB and OmA observation counts are nearly identical and therefore the lines overlap sufficiently to be indistinguishable.

CONUS domain, and thus increasing the number of scattering particles for the radar(s). Additionally, super-observation processing over smaller spatial and temporal box sizes results in a larger number of total super-observations. For example, the control and w_incl assimilate the same number of super-observations (e.g., Fig. 10d red line versus black line) since there is no change to the super-observation parameters. There are more super-observations in w_so_elev5 due to the reduction in super-observation box sizes, thus allowing for more super-observation boxes (e.g., Fig. 7). By raising the elevation angle from 5° to 10° in experiments w_so_elev10 and so_elev10, there is an additional increase in the observation counts. The two elev_10 experiments (e.g., Fig. 10d blue line versus purple line) assimilate the same number of super-observations

since the only difference between those experiments is related to the observation operator.

A direct comparison of RMS and bias values cannot be made between experiments with differing super-observations parameters due to sensitivities related to changing the underlying characteristics of the super-observations themselves (e.g., differing sample sizes as noted in the prior paragraph). For example, changing the degree of super-observation processing, by changing the spatial box size and time window length, will change the statistics within the super-observation box (e.g., variance). This effect is then compounded from the use of data assimilation cycling and complicates the ability to interpret the results between experiments using differing super-observation parameter settings. Therefore, only two comparisons
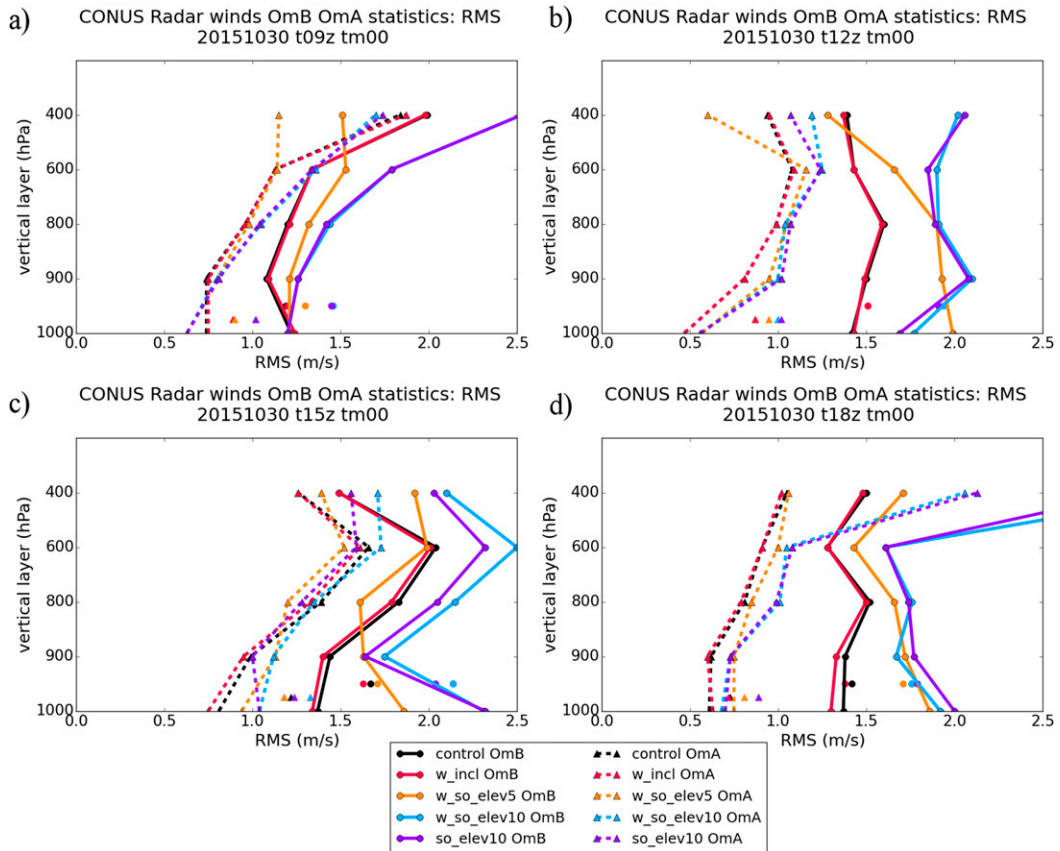
FIG. 11. Root-mean-square (RMS) error from the GSI observation minus background (OmB; circles/solid line) and observation minus analysis (OmA; triangles/dashed lines) statistics files over entire CONUS nest domain for the forecast cycles (a) 0000, (b) 0600, (c) 1200, and (d) 1800 UTC 30 Oct 2015. The individual circle/triangle markers along the *x* axis denote the aggregate values for the total CONUS atmosphere.

will be made, both of which only consider the effects of including vertical velocity in the observation operator: control versus w_incl and so_elev10 versus w_so_elev10.

There is an overall neutral impact on the OmB/OmA RMS (Fig. 11) and bias (Fig. 12) as a result of extending the forward operator to include *w*. The OmB RMS and bias for experiment w_so_elev10 (w_incl) have little to no differences compared to the counterpart experiment so_elev10 (the control). Based on this limited dataset, there is no consistent improvement or degradation in the RMS and bias of the fit-to-observations for differences as a result of the improved observation operator. In general, the OmB RMS/bias values are larger than their corresponding OmA RMS/bias for each experiment; which is expected.

b. Forecast assessment

To assess the impacts on the resulting forecasts, we begin with a qualitative comparison of forecasts of accumulated precipitation from the 1200 UTC initialization

time on 30 October 2015 (Fig. 13). This is followed by an assessment of FSS and FBIAS scores from forecasts initialized at 0900, 1200, 1500, and 1800 UTC 30 October 2015 (Figs. 14 and 15). Each experiment (refer to Table 3) was tested for statistical significance at the 90% level using bootstrap confidence intervals constructed from 2000 replications on the difference curves computed relative to the control simulation. Statistical significance is found where the confidence intervals do not encompass zero. Statistics are considered only over the approximate region that experienced heavy rainfall, which is a broad area covering the southern CONUS (Fig. 2; gray shaded). Further, FSS statistics are summarized across several thresholds and box sizes via the use of a so-called scorecard (Fig. 16).

The control (Fig. 13b) simulated a much larger area of very heavy precipitation located near central Texas as compared to observations (Fig. 13a) and compared to the experiments with modified super-observation parameters (Figs. 13d–f, respectively). The changes in the coverage of the heavy precipitation can be noted
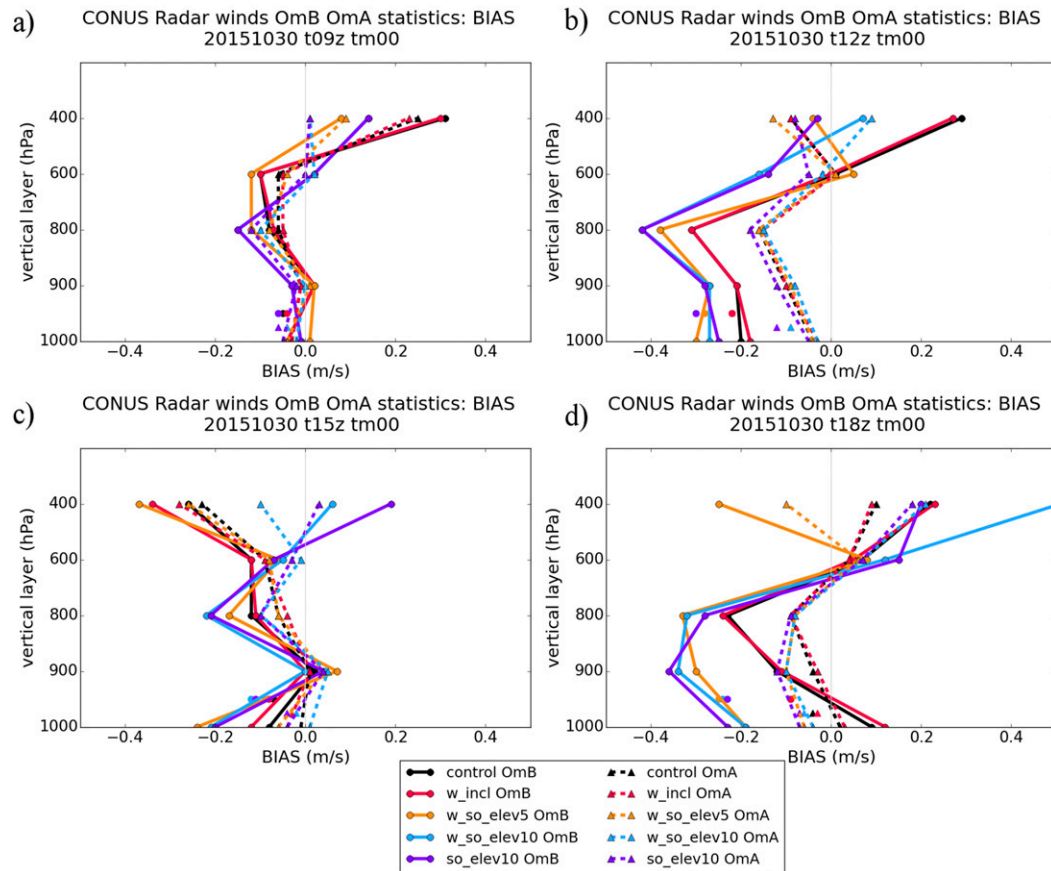
FIG. 12. Bias from the GSI observation minus background (OmB; circles/solid line) and observation minus analysis (OmA; triangles/dashed lines) statistics files over entire CONUS nest domain for the forecast cycles (a) 0000, (b) 0600, (c) 1200, and (d) 1800 UTC 30 Oct 2015. The individual circle/triangle markers along the x axis denote the aggregate values for the total CONUS atmosphere.

by the 3 in. contour (Fig. 13 bold black line). The over-prediction of the precipitation is reduced in this area when the super-observation parameters were adjusted, suggesting some sensitivity to the super-observation processing. There appears to be qualitatively little-to-no impact made when vertical velocity was included in the observation operator when comparing against the control (experiment w_incl; Fig. 13b). The FSS (Fig. 14) and FBIAS (Fig. 15a) difference scores support this mostly neutral change as the control (black) and w_incl (red) lines are consistently very similar among all metrics and thresholds, with the exception of FBIAS degradation at 0.10 and 0.25 in. and an improvement at 1.00 in. The scorecard (Fig. 16) shows that the difference between w_incl and the control is slightly degraded for the lower thresholds (e.g., 0.01, 0.05, and 0.10 in.) at all box sizes and slightly improved for the higher thresholds (e.g., 0.50 and 1.00 in.).

There was a slightly more distinct impact in w_so_elev5 (Fig. 13d), as compared to the control and the w_incl

experiments. In experiment w_so_elev5, the spatial coverage of the wet bias of the precipitation bullseye near Austin was reduced. While the wet bias in this region was reduced, the placement of precipitation was slightly eastward of the observed location. The w_so_elev5 FSS (Fig. 14) difference scores show similar but larger impacts to that of experiment w_incl. Slight degradation (improvement) is found for the lower (higher) thresholds. For FBIAS (Fig. 15a) there is degradation at thresholds 0.01 and 0.05 in. [i.e., increasing the wet bias of control (Fig. 15b)], and a trend toward improvements at thresholds 0.50 and 1.00 in. The scorecard (Fig. 16) shows w_so_elev5 to have a similar pattern to w_incl, but there is less degradation at the low thresholds and stronger improvements at higher thresholds. There is an overall slight improvement for all box sizes and all thresholds as compared to w_incl.

The w_so_elev10 and so_elev10 experiments (Figs. 13e and 13f, respectively), having similar forecasts, further
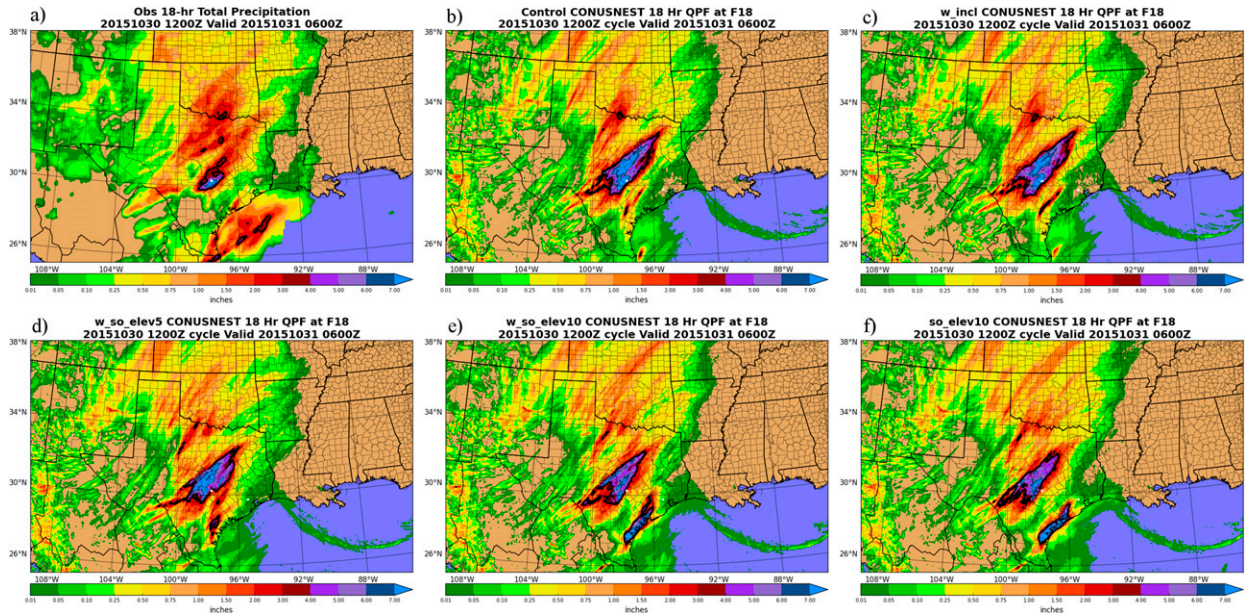
FIG. 13. 18-h accumulated precipitation for the period 1200 UTC 30 Oct–0600 UTC 31 Oct 2015. (a) The observations and the experiments are (b) control, (c) w_incl, (d) w_so_elev5, (e) w_so_elev10, and (f) so_elev10. The white dot (30.27°N, 97.74°W) denotes the location of Austin, TX, and the white dot (29.76°N, 95.37°W) denotes the location of Houston, TX. The black contour denotes the area of 3 in.

reduce spatial coverage of the precipitation bullseye as compared to w_so_elev5. The elev10 experiments appear to have the subjectively better overall forecasts as the broad wet-bias in the central part of Texas appears improved and more closely reflects the extent and magnitude seen in observations. While both experiments still miss the heavy rain in southeast Texas extending over the Gulf, they do reflect heavy precipitation in the region associated with rotating storms that occurred later in the period (discussed in section 3c),
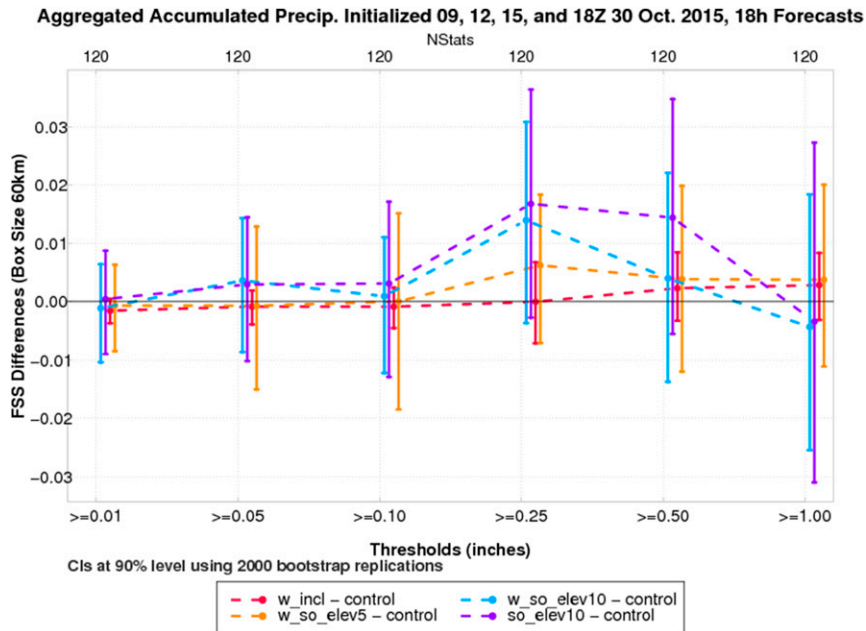

FIG. 14. Fractions skill score (FSS) differences from control for 3-h precipitation forecasts out to 18 h aggregated from 3-hourly forecasts initialized beginning at 0900, 1200, 1500, and 1800 UTC 30 Oct 2015.
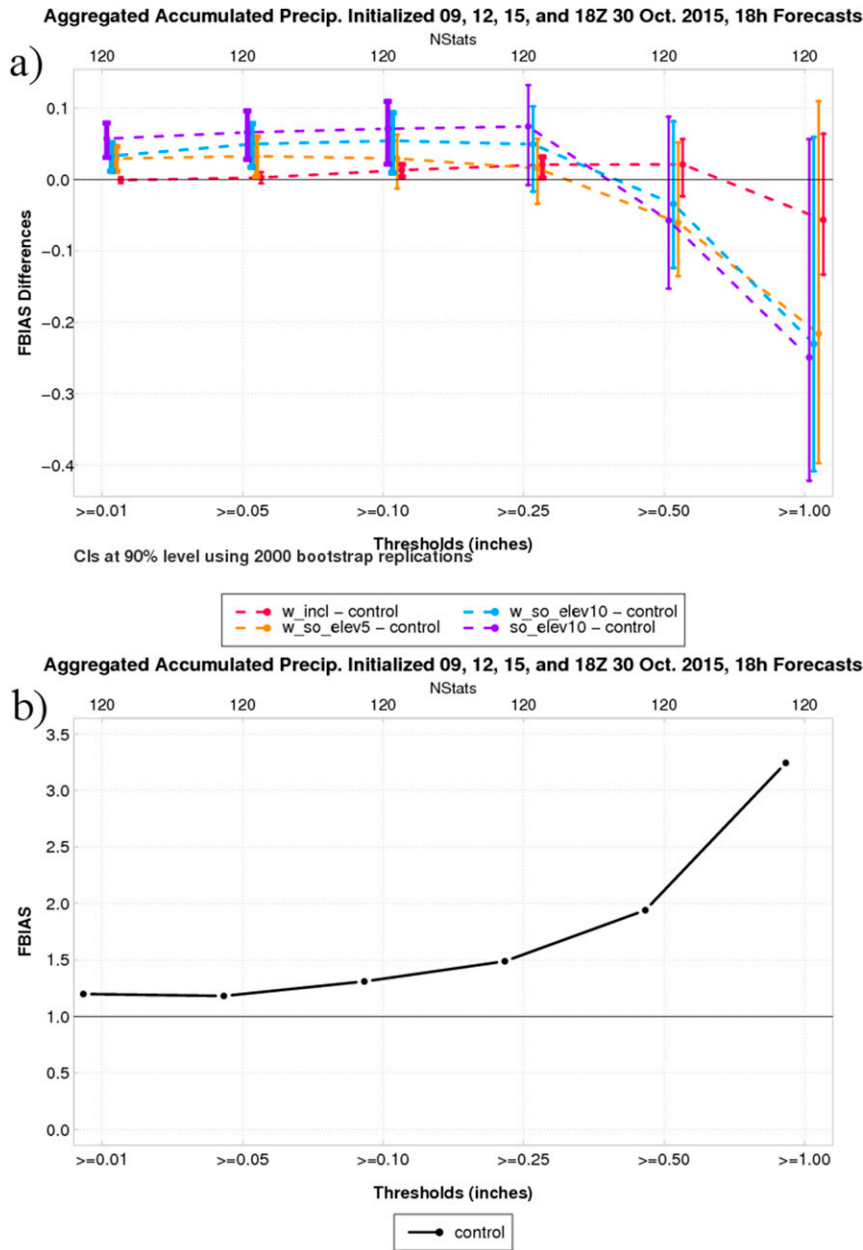
FIG. 15. Frequency bias (FBIAS) difference from (a) control and (b) the control FBIAS values for 3-h precipitation forecasts out to 18 h aggregated from 3-hourly forecasts initialized beginning at 0900, 1200, 1500, and 1800 UTC 30 Oct 2015.

unlike the control and w_incl. The FSS statistics (Fig. 14) confirm the positive forecast impact at 0.25 and 0.50 in. but slight degradation at 1.00 in. The FBIAS statistics (Fig. 15a) show a reduction in wet bias for the 0.50 and 1.00 in. thresholds. From this set of experiments, there is not a clear signal that suggests that including vertical velocity provides a statistically significant advantage. The largest improvements may be attributed to the enhanced super-observation settings

with raised elevation angles, in the margins of statistical significance.

The experiments with modified super-observation parameters tended to have the greatest positive impact on the forecast. The extension of vertical velocity to the observation operator was found to have mostly neutral impacts in combination with the modified super-observation parameters (Fig. 16). The three super-observation experiments exhibited heavy precipitation

Fraction Skill Score Differences (Experiment minus Control)
Accumulated Precip. Initialized 09-18Z 30 Oct. 2015, 18h Forecasts

Threshold (in.)	10	20	30	40	50	60	70	80	90	100	
≥ 1.00	0.001	0.001	0.002	0.002	0.003	0.003	0.003	0.003	0.003	0.003	w_incl
≥ 0.50	0.003	0.003	0.003	0.003	0.003	0.002	0.002	0.002	0.001	0.001	
≥ 0.25	0.001	0.001	0.001	0.001	0.000	0.000	0.000	-0.001	-0.001	-0.002	
≥ 0.10	-0.001	-0.001	-0.001	-0.001	-0.001	-0.001	-0.001	-0.001	-0.001	-0.001	
≥ 0.05	-0.001	-0.001	-0.001	-0.001	-0.001	-0.001	-0.001	-0.001	-0.001	-0.001	
≥ 0.01	-0.001	-0.002	-0.002	-0.002	-0.002	-0.002	-0.002	-0.002	-0.002	-0.002	
≥ 1.00	0.000	0.001	0.001	0.002	0.003	0.004	0.004	0.005	0.006	0.007	w_so_elev5
≥ 0.50	0.000	0.000	0.001	0.002	0.003	0.004	0.005	0.006	0.007	0.008	
≥ 0.25	0.008	0.008	0.008	0.007	0.007	0.006	0.006	0.005	0.005	0.004	
≥ 0.10	0.002	0.002	0.001	0.001	0.000	0.000	0.000	-0.001	-0.001	-0.002	
≥ 0.05	0.000	0.000	0.000	0.000	-0.001	-0.001	-0.001	-0.001	-0.001	-0.002	
≥ 0.01	0.000	0.000	0.000	0.000	-0.001	-0.001	-0.001	-0.001	-0.001	-0.001	
≥ 1.00	-0.006	-0.006	-0.005	-0.005	-0.005	-0.004	-0.004	-0.003	-0.003	-0.002	w_so_elev10
≥ 0.50	0.002	0.002	0.002	0.003	0.003	0.004	0.005	0.005	0.006	0.006	
≥ 0.25	0.013	0.013	0.014	0.014	0.014	0.014	0.014	0.014	0.014	0.014	
≥ 0.10	0.002	0.002	0.002	0.001	0.001	0.001	0.001	0.001	0.000	0.000	
≥ 0.05	0.004	0.004	0.004	0.004	0.004	0.004	0.004	0.003	0.003	0.003	
≥ 0.01	0.000	0.000	0.000	-0.001	-0.001	-0.001	-0.001	-0.002	-0.002	-0.002	
≥ 1.00	-0.006	-0.005	-0.004	-0.004	-0.004	-0.003	-0.003	-0.003	-0.002	-0.001	so_elev10
≥ 0.50	0.008	0.009	0.010	0.012	0.013	0.014	0.016	0.017	0.018	0.019	
≥ 0.25	0.014	0.015	0.016	0.016	0.017	0.017	0.017	0.017	0.017	0.016	
≥ 0.10	0.004	0.004	0.003	0.003	0.003	0.003	0.003	0.003	0.003	0.002	
≥ 0.05	0.004	0.004	0.003	0.003	0.003	0.003	0.003	0.003	0.002	0.002	
≥ 0.01	0.001	0.001	0.001	0.001	0.001	0.000	0.000	0.000	0.000	-0.001	

Box size (km)

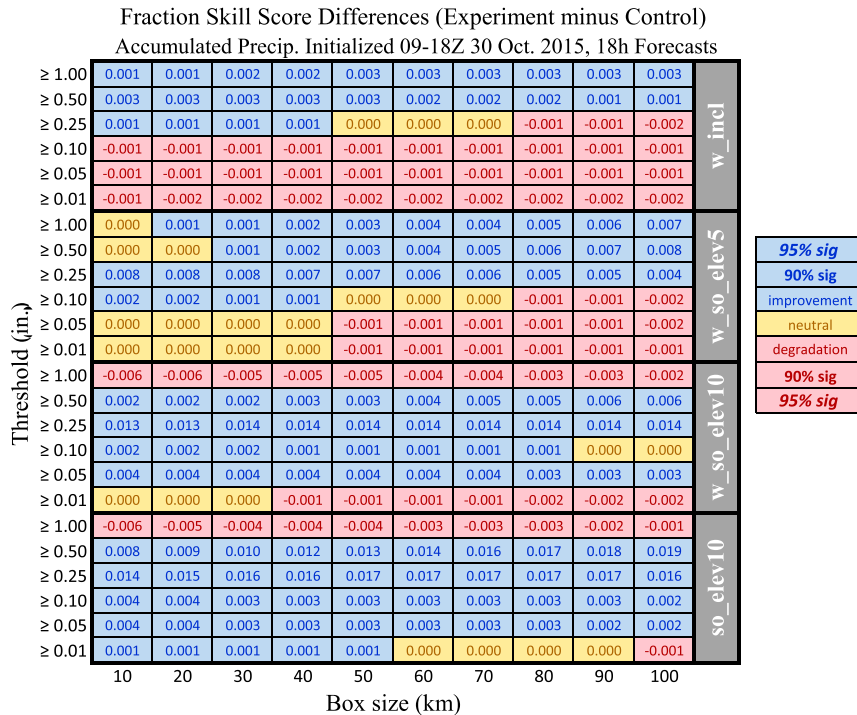Legend: *95% sig* / **90% sig** / improvement / neutral / degradation / **90% sig** / **95% sig**

FIG. 16. Fractions skill score (FSS) scorecard for the differences between the control and each experiment for various accumulated precipitation thresholds and box sizes. Improvements and degradations are shown, rounded to three decimal places, with the corresponding statistical significance at the 90% and 95% confidence intervals.

located near Houston (Figs. 13d,e,f) with increasing magnitudes when higher elevation angles were included. This is an important distinction because there was a marked increase in simulated storm rotation correlating to the locations of tornado reports.

c. Houston, Texas, region precipitation

Here we discuss the aspects of the experimental configurations that led to the differences in precipitation forecasts along the Texas Gulf Coast and into Houston and use tornado reports as a proxy for storms with rotating updrafts.

Figure 9 notes the time and date of each tornado report for the 1200 UTC 30 October–1159 UTC 31 October forecast period; the earliest tornado report in the Houston region occurred after 0900 UTC 31 October 2015. According to observed radar reflectivity, the storms associated with the tornado reports in the Houston area initiated just off the coast of Port O'Connor, Texas, around 0300 UTC 31 October 2015. The storms traveled northeastward into the Houston area where several tornadoes occurred. This discussion will focus on the 1200 UTC initialized forecast performance with a focus on the updraft helicity forecasts near Houston.

The 1200 UTC initialized super-observation experiments, especially so_elev10 and w_so_elev10 all predicted heavy precipitation along the Texas Gulf Coast beginning near Port O'Connor and extending into the Houston region. This is a major difference between these experiments and the non-super-observation experiments as the non-super-observation experiments were *not* able to capture the initiation and life cycle of the storms associated with the warm frontal boundary (Fig. 17a) and low-level jet. As it was noted before, the storms in this region initiated around 0300 UTC 31 October 2015 while the super-observation experiments tended to have a much earlier initiation of several hours (e.g., 6 + hours) prior to verification. The elev10 experiments clearly predicted strong, rotating storms (Figs. 18c–f) to occur in the location that was being monitored by the Storm Prediction Center (Fig. 17a) and more closely corresponds to the locations of the observed tornado reports (Fig. 9) in the Houston area as well as with observed radar reflectivity (Fig. 18h). The control run predicted storms from 1900 to 0000 UTC 31 October (Figs. 18a,b) that were associated with interaction with the warm front. Those storms were less organized and less persistent as compared to the modified super-observation parameter experiments.
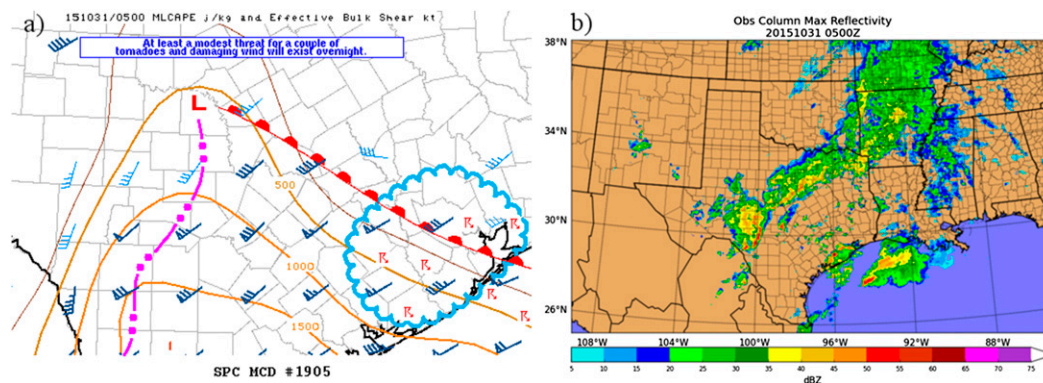
FIG. 17. Storm prediction center mesoscale analysis for 0500 UTC 31 Oct 2015 (available online at http://www.spc.noaa.gov/exper/archive/event.php?date=20151030) accompanied by observed reflectivity valid at the same time.

The forecasts are clearly sensitive to the super-observation parameters. The super-observation settings were modified to average observations over a smaller spatial box and temporal window; therefore, there were fewer observations per super-observation box and thus a lesser degree of smoothing of the observations. By smoothing over smaller spatial and temporal windows, there were was a greater density of total super-observations assimilated where each was more representative of the raw form of the observations occurring at the time of assimilation. The demonstrated sensitivity indicates that the operational super-observation settings (i.e., those used in the control) smoothes the observations to a greater degree than necessary and discards potentially useful information. Averaging over a long time period may also have the undesirable impact of dampening significant convective-scale motions (e.g., situations when the observations change rapidly at subhourly time intervals). The modified configuration used within this study, however, may not necessarily be the optimal configuration for these parameters but identifies sensitivities that result in potential forecast improvement thus forming a foundation for continued development toward improving the assimilation of these data.

d. Forecast sensitivity to background error covariance length scales

The three experiments that feature vertical velocity in the observation operator: w_incl, w_so_elev5, and w_so_elev10 were also run with the same global constant background error covariance $0.7 \, m^2 \, s^{-2}$ but different horizontal and vertical length scale: 100-km and 1-grid units, respectively. These values correspond to default values that may be used by the GSI. The forecast impacts were also assessed for this new set of experiments using the 18-h total accumulated precipitation

plot from the 1200 UTC cycle and the corresponding FSS stats summarized by a scorecard for multiple thresholds and box sizes (not shown). The experiments that featured vertical velocity in the observation operator and as an analysis control variable were rerun to demonstrate that there is a forecast sensitivity to these parameters despite that the fact that vertical velocity is a diagnostic variable in the NMMB. Future research should consider generating new background statistics when considering analyzing vertical velocity and that the results of this study are not conclusive to the importance or lack thereof of including vertical velocity. There was consistency in results that modifying the super-observation parameters improved the results.

4. Summary and conclusions

The radial wind observation operator in the GSI was extended to include vertical velocity and testing associated with the refinement of the radial wind super-observation processing was performed in a single case study. To evaluate the impacts of this extension, experimental configurations using an hourly configuration of the NAMv4 data assimilation and model framework was used beginning at 0000 UTC 30 October and ran through 0000 UTC 31 October 2015. The data assimilation consists of a hybrid 3DEnVar data assimilation system which uses the hydrostatic GDAS ensemble Kalman filter (~35-km) for the ensemble contribution. The NAMv4 was run using a 12-km parent domain and 3-km CONUS nest domain with the verification run on a 5-km grid.

The experiments started with the control which mimics the operational configuration with relaxed quality control parameters for the radial wind observations. Incremental modifications to the experimental setup followed by adding vertical velocity to the forward
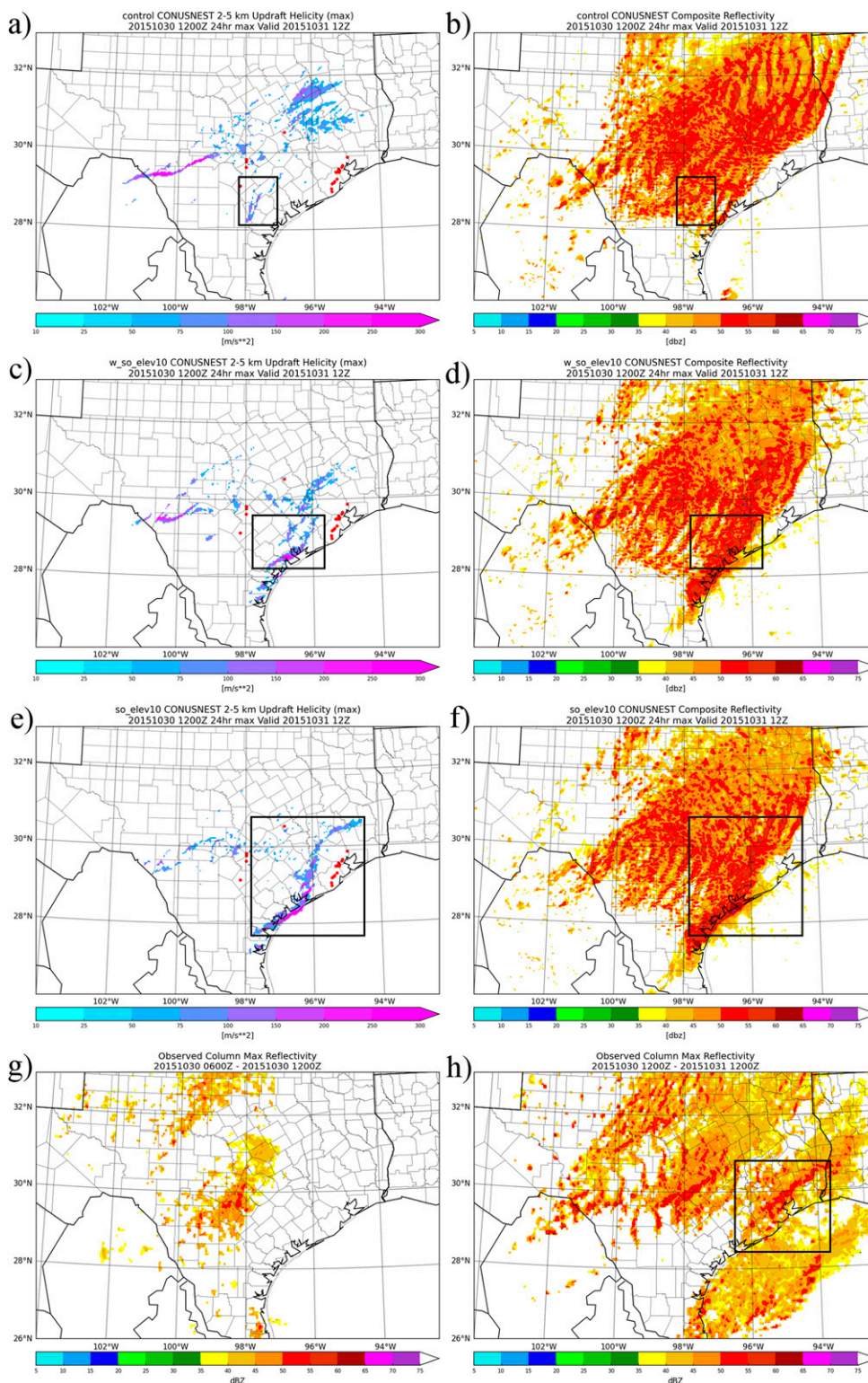
FIG. 18. The 1200 UTC initialized, 24-h maximum updraft helicity (UH: masked below $50 \, \mathrm{m \, s^{-2}}$) and radar reflectivity (masked below 35 dBZ) valid at 1200 UTC 31 Oct 2015 for (a),(b) control, (c),(d) w_so_elev10, and (e),(f) so_elev10, respectively. For reference, the max radar reflectivity for the (g) convectively active regions during the 6 h data assimilation period (0600–1200 UTC), and (h) the 24-h forecast period are also shown. The updraft helicity that is boxed corresponds to the storms that developed at the intersection of the LLJ and warm front boundary (Fig. 17a) and the storms that produced tornadoes [tornado reports: red dots on (a), (c), and (e)].

operator, adjusting some of the super-observation parameters, and finally, adjusting the maximum elevation angle to 10°. The experiments were evaluated using objective analyses of accumulated precipitation using categorical and neighborhood verification metrics aggregated for 18-h forecasts over the 0900, 1200, 1500, and 1800 UTC 30 October 2015 forecast cycles to accommodate the 3-h precipitation observation buckets. A constant value of $0.7 \, \mathrm{m^2 \, s^{-2}}$ was used for the background error covariance for vertical velocity and a horizontal and vertical scale of influence of 27 km and 10 grid units, respectively, in the main set of experiments. These values were chosen based on preliminary testing and tuning; however, future studies should generate a new background error covariance which includes vertical velocity.

The fit-to-observations were used to assess the impact to the data assimilation system between experiments with differences only related to the radial wind observation operator. For example, the RMS innovation from the GSI observation minus background and analysis for the control was compared with w_incl and experiment so_elev10 was compared with w_so_elev10. The RMS scores showed a neutral impact on the analysis for including vertical velocity in the observation operator.

Quantitative results for the elev10 experiments showed slight improvements in the FSS of box size 60 km for accumulated precipitation at the 0.25 and 0.50 in. thresholds and in frequency bias at the 0.50 and 1.00 in. thresholds (Figs. 14 and 15). There was a slight degradation in the lower FBIAS thresholds. A summary of FSS statistics across a variety of thresholds and scales were also presented in a scorecard (Fig. 16). Results from the scorecard demonstrated that the strongest sensitivity was to the super-observation parameters where those experiments mostly demonstrated some (slight) improvement relative to the control. No results showed statistical significance.

Because the model is not directly forced by the analysis of vertical velocity, the results from these experiments can be attributed to two factors: 1) reducing the error associated with the original Doppler radar radial wind forward operator via the inclusion of vertical velocity and 2) refining the super-observation parameters and adjusting the maximum elevation angle. The most impactful changes resulting in forecast improvement were associated with the refined super-observation procedure in conjunction with the adjustment to the max elevation angle.

The elev10 experiments (w_so_elev10 and so_elev10) predicted a band of high precipitation accumulations along the Texas Gulf Coast that was not present in the control or w_incl experiment. This band of heavy precipitation corresponds to a simulated storm(s) with rotating updrafts. These model simulated storms matched closer to the location of observed tornado reports and hence storms with rotating updrafts but still displaced ~100 km to the west.

There is support that the elev10 experiments showed the greatest improvements to the forecast of accumulated precipitation (Fig. 16) and demonstrated a more accurate forecast of updraft helicity swaths corresponding to tornado reports (Fig. 18). These findings suggest that convective-scale model forecasts are sensitive to the methods and settings for assimilating radial winds.

Testing in an ideal framework revealed that errors of up to $1 \, \mathrm{m \, s^{-1}}$ could be expected for elevation angles around 10° and vertical motions of $10 \, \mathrm{m \, s^{-1}}$ (Fig. 3). However, the results of this study appear contradictory; the impact of adding vertical velocity to the forward operator was effectively negligible. This result is likely due to several factors which limits the generality of the findings. Such limiting factors likely include: the lack of a convective-scale ensemble in the hybrid 3DEnVar algorithm, the treatment of vertical velocity as a sink term in the analysis, limitations to a single case, and frequency of assimilation of radial wind observations.

A second set of experiments that featured vertical velocity in the observation operator and as a control variable were run using the same background error covariance but a horizontal and vertical scale of influence of 100 km and 1 grid units, respectively. This additional set of experiments showed mixed results and that the tuning of the background error covariance statistics play a crucial role in obtaining positive forecast impacts even while using a nonhydrostatic model without a fully prognostic term for vertical velocity.

The results of this work are to be considered as first steps toward refining and improving the use of these abundant, convective-scale data. There are additional areas of convective-scale data assimilation to be explored in an operational context, such as the use of a convective-scale ensemble and a more impactful use of the analysis of vertical velocity instead of limiting it to a sink term in the observation operator. These experiments also only featured hourly data assimilation updates while trying to characterize features that evolve on subhourly time scales. Finally, future work toward expanding these tests to additional cases will likely yield more conclusive results.

and the Environmental Modeling Center as well as in partial fulfillment of graduate work at the University of Maryland, College Park. The authors acknowledge the NOAA Research and Development High-Performance Computing Program for providing computing and storage resources that have contributed to the research results reported within this paper (http://rdhpcs.noaa.gov). The authors thank Drs. Shun Liu and Manuel Pondeca for reviews of an earlier version of this manuscript. Drs. Wan-Shu Wu and Ting Lei are also thanked for their helpful discussions. Three anonymous reviewers are thanked for their help in improving this manuscript.

REFERENCES

Aligo, E. A., B. Ferrier, and J. R. Carley, 2018: Modified NAM microphysics for forecasts of deep convective storms. *Mon. Wea. Rev.*, **146**, 4115–4153, https://doi.org/10.1175/MWR-D-17-0277.1.

Alpert, J. C., 2004: Sub-grid scale mountain blocking at NCEP. Preprints, *20th Conf. on Weather Analysis and Forecasting/16th Conf. on Numerical Weather Prediction*, Seattle, WA, Amer. Meteor. Soc., P2.4, https://ams.confex.com/ams/pdfpapers/71011.pdf.

——, and V. K. Kumar, 2007: Radial wind super-obs from the WSR-88D radars in the NCEP operational assimilation system. *Mon. Wea. Rev.*, **135**, 1090–1109, https://doi.org/10.1175/MWR3324.1.

Crum, T. D., and R. L. Alberty, 1993: The WSR-88D and the WSR-88D operational support facility. *Bull. Amer. Meteor. Soc.*, **74**, 1669–1687, https://doi.org/10.1175/1520-0477(1993)074<1669:TWATWO>2.0.CO;2.

De Pondeca, Manuel S. F. V., and Coauthors 2011: The real-time mesoscale analysis at NOAA's National Centers for Environmental Prediction: Current status and development. *Wea. Forecasting*, **26**, 593–612, https://doi.org/10.1175/WAF-D-10-05037.1.

Djalalova, I. V., and Coauthors, 2016: The POWER experiment: Impact of assimilation of a network of coastal wind profiling radars on simulating offshore winds in and above the wind turbine layer. *Wea. Forecasting*, **31**, 1071–1091, https://doi.org/10.1175/WAF-D-15-0104.1.

Duda, J. D., X. Wang, Y. Wang, and J. R. Carley, 2019: Comparing the assimilation of radar reflectivity using the direct GSI-based ensemble–variational (EnVar) and indirect cloud analysis methods in convection-allowing forecasts over the continental United States. *Mon. Wea. Rev.*, **147**, 1655–1678, https://doi.org/10.1175/MWR-D-18-0171.1.

Ek, M. B., K. E. Mitchell, Y. Lin, E. Rogers, P. Grunmann, V. Koren, G. Gayno, and J. D. Tarpley, 2003: Implementation of Noah land surface model advances in the National Centers for Environmental Prediction operational mesoscale Eta model. *J. Geophys. Res.*, **108**, 8851, https://doi.org/10.1029/2002JD003296.

Fabry, F., 2010: Radial velocity measurement simulations: Common errors, approximations, or omissions and their impact on estimation accuracy. *Proc. Sixth European Conf. on Radar in Meteorology and Hydrology*, Sibiu, Romania, ERAD, 17.2.

Gao, J., and D. J. Stensrud, 2014: Some observing system simulation experiments with a hybrid 3DEnVAR system for storm-scale radar data assimilation. *Mon. Wea. Rev.*, **142**, 3326–3346, https://doi.org/10.1175/MWR-D-14-00025.1.

——, M. Xue, K. Brewster, and K. K. Droegemeier, 2004: A three-dimensional variational data analysis method with recursive filter for Doppler radars. *J. Atmos. Oceanic Technol.*, **21**, 457–469, https://doi.org/10.1175/1520-0426(2004)021<0457:ATVDAM>2.0.CO;2.

Ge, G., J. Gao, K. Brewster, and M. Xue, 2010: Impacts of beam broadening and Earth curvature on storm-scale 3D variational data assimilation of radial velocity with two Doppler radars. *J. Atmos. Oceanic Technol.*, **27**, 617–636, https://doi.org/10.1175/2009JTECHA1359.1.

Gustafsson, N., and Coauthors, 2018: Survey of data assimilation methods for convective-scale numerical weather prediction at operational centres. *Quart. J. Roy. Meteor. Soc.*, **144**, 1218–1256, https://doi.org/10.1002/qj.3179.

Holleman, I., H. Benschop, and J. van der Meulen, 2005: Upper air wind measurements by weather radar. *WMO Tech. Conf. on Meteorological and Environmental Instruments and Methods of Observation (TECO 2005)*, Bucharest, Romania, WMO, https://www.wmo.int/pages/prog/www/IMOP/publications/IOM-82-TECO_2005/Papers/2(05)_Netherlands_5_Holleman.pdf.

Hu, M., S. G. Benjamin, T. T. Ladwig, D. C. Dowell, S. S. Weygandt, C. R. Alexander, and J. S. Whitaker, 2017: GSI three-dimensional ensemble–variational hybrid data assimilation using a global ensemble for the regional Rapid Refresh model. *Mon. Wea. Rev.*, **145**, 4205–4225, https://doi.org/10.1175/MWR-D-16-0418.1.

Iacono, M. J., J. S. Delamere, E. J. Mlawer, M. W. Shephard, S. A. Clough, and W. D. Collins, 2008: Radiative forcing by long-lived greenhouse gasses: Calculations with the AER radiative transfer models. *J. Geophys. Res.*, **113**, D13103, https://doi.org/10.1029/2008JD009944.

Ishikawa, Y., and K. Koizumi, 2006: Doppler radar wind data assimilation with the JMA meso 4D-Var. WMO WGNE Research Activities in Atmosphere and Oceanic Modeling 2006, Rep. 36, Section 01, 11–12, https://www.wcrp-climate.org/WGNE/BlueBook/2006/individual-articles/01_Ishikawa_Yoshihiro_Doppler_Meso_4D-Var.pdf.

Janjić, Z. I., 1994: The step-mountain Eta coordinate model: Further developments of the convection, viscous sublayer, and turbulence closure schemes. *Mon. Wea. Rev.*, **122**, 927–945, https://doi.org/10.1175/1520-0493(1994)122<0927:TSMECM>2.0.CO;2.

——, 2001: Nonsingular implementation of the Mellor-Yamada level 2.5 scheme in the NCEP meso model. NCEP Office Note 437, 91 pp.

——, and R. Gall, 2012: Scientific documentation of the NCEP Nonhydrostatic Multiscale Model on the B-grid (NMMB). Part 1: Dynamics. NCAR Tech. Note NCAR/TN-489+STR, https://doi.org/10.5065/D6WH2MZX.

Janjić, T., and Coauthors, 2018: On the representation error in data assimilation. *Quart. J. Roy. Meteor. Soc.*, **144**, 1257–1278, https://doi.org/10.1002/qj.3130.

Johnson, A., X. Wang, J. R. Carley, L. J. Wicker, and C. Karstens, 2015: A comparison of multiscale GSI-based EnKF and 3DVar data assimilation using radar and conventional observations for midlatitude convective-scale precipitation forecasts. *Mon. Wea. Rev.*, **143**, 3087–3108, https://doi.org/10.1175/MWR-D-14-00345.1.

Kleist, D. T., and K. Ide, 2015: An OSSE-based evaluation of hybrid variational–ensemble data assimilation for the NCEP GFS. Part I: System description and 3D-hybrid

results. *Mon. Wea. Rev.*, **143**, 433–451, https://doi.org/10.1175/MWR-D-13-00351.1.

——, D. F. Parrish, J. C. Derber, R. Treadon, W.-S. Wu, and S. Lord, 2009: Introduction of the GSI into the NCEP global data assimilation system. *Wea. Forecasting*, **24**, 1691–1705, https://doi.org/10.1175/2009WAF2222201.1.

Lin, Y., and K. E. Mitchell, 2005: The NCEP stage II/IV hourly precipitation analyses: Development and applications. *19th Conf. on Hydrology*, San Diego, CA, Amer. Meteor. Soc., 1.2, https://ams.confex.com/ams/Annual2005/techprogram/paper_83847.htm.

Lindskog, M., K. Salonen, H. Järvinen, and D. B. Michelson, 2004: Doppler radar wind data assimilation with HIRLAM 3DVar. *Mon. Wea. Rev.*, **132**, 1081–1092, https://doi.org/10.1175/1520-0493(2004)132<1081:DRWDAW>2.0.CO;2.

Lippi, D. E., D. T. Kleist, and J. R. Carley, 2016: Assimilation of radar radial velocity with GSI-based hybrid 3DEnVar system for improved precipitation forecasts. M.S. scholarly paper, Dept. of Atmospheric and Oceanic Science, University of Maryland, 45 pp. https://www.atmos.umd.edu/theses_archive/.

Liu, S., and Coauthors, 2016: WSR-88D radar data processing at NCEP. *Wea. Forecasting*, **31**, 2047–2055, https://doi.org/10.1175/WAF-D-16-0003.1.

——, M. Xue, J. Gao, and D. Parrish, 2005: Analysis and impact of super-obbed Doppler radial velocity in the NCEP Grid-point Statistical Interpolation (GSI) analysis system. Preprints, *21st Conf. on Weather Analysis and Forecasting/17th Conf. on Numerical Weather Prediction,* Washington, DC, Amer. Meteor. Soc., 13A.4, https://ams.confex.com/ams/WAFNWP34BC/techprogram/paper_94230.htm.

Lorenc, A. C., 2003: The potential of the ensemble Kalman filter for NWP—A comparison with 4DVar. *Quart. J. Roy. Meteor. Soc.*, **129**, 3183–3203, https://doi.org/10.1256/qj.02.132.

——, 2013: Recommended nomenclature for EnVar data assimilation methods. *Research Activities in Atmospheric and Oceanic Modeling,* WGNE, 2 pp., http://www.wcrp-climate.org/WGNE/BlueBook/2013/individual-articles/01_Lorenc_Andrew_EnVar_nomenclature.pdf.

Mlawer, E. J., S. J. Taubman, P. D. Brown, M. J. Iacono, and S. A. Clough, 1997: Radiative transfer for inhomogeneous atmospheres: RRTM, a validated correlated-k model for the longwave. *J. Geophys. Res.*, **102**, 16 663–16 682, https://doi.org/10.1029/97JD00237.

Parrish, D. F., and J. C. Derber, 1992: The National Meteorological Center's Spectral Statistical-Interpolation analysis system. *Mon. Wea. Rev.*, **120**, 1747–1763, https://doi.org/10.1175/1520-0493(1992)120<1747:TNMCSS>2.0.CO;2.

Peckham, S. E., T. G. Smirnova, S. G. Benjamin, J. M. Brown, and J. S. Kenyon, 2016: Implementation of a digital filter initialization in the WRF Model and its application in the Rapid Refresh. *Mon. Wea. Rev.*, **144**, 99–106, https://doi.org/10.1175/MWR-D-15-0219.1.

Purser, R. J., W.-S. Wu, D. F. Parrish, and N. M. Roberts, 2003a: Numerical aspects of the application of recursive filters to variational statistical analysis. Part I: Spatially homogeneous and isotropic Gaussian covariances. *Mon. Wea. Rev.*, **131**, 1524–1535, https://doi.org/10.1175//1520-0493(2003)131<1524:NAOTAO>2.0.CO;2.

——, ——, ——, and ——, 2003b: Numerical aspects of the application of recursive filters to variational statistical analysis. Part II: Spatially inhomogeneous and anisotropic general covariances. *Mon. Wea. Rev.*, **131**, 1536–1548, https://doi.org/10.1175//2543.1.

Rihan, F. A., C. G. Collier, S. P. Ballard, and S. J. Swarbrick, 2008: Assimilation of Doppler radial winds into a 3D-Var system: Errors and impact of radial velocities on the variational analysis and model forecasts. *Quart. J. Roy. Meteor. Soc.*, **134**, 1701–1716, https://doi.org/10.1002/qj.326.

Roberts, N. M., and H. W. Lean, 2008: Scale-selective verification of rainfall accumulations from high-resolution forecasts of convective events. *Mon. Wea. Rev.*, **136**, 78–97, https://doi.org/10.1175/2007MWR2123.1.

Rogers, E., and Coauthors, 2017: Upgrades to the NCEP North American Mesoscale (NAM) system. *Working Group on Numerical Experimentation Blue Book*, 2 pp., http://wmc.meteoinfo.ru/bluebook/uploads/2017/docs/05_Rogers_Eric_mesoscale_modeling.pdf.

Simonin, D., S. P. Ballard, and Z. Li, 2014: Doppler radar radial wind assimilation using an hourly cycling 3DVar with a 1.5 km resolution version of the Met Office Unified Model for nowcasting. *Quart. J. Roy. Meteor. Soc.*, **140**, 2298–2314, https://doi.org/10.1002/qj.2298.

Spilhaus, A. F., 1948: Raindrop size, shape, and falling speed. *J. Meteor.*, **5**, 108–110, https://doi.org/10.1175/1520-0469(1948)005<0108:RSSAFS>2.0.CO;2.

Waller, J. A., D. Simonin, S. L. Dance, N. K. Nichols, and S. P. Ballard, 2016: Diagnosing observation error correlations for Doppler radar radial winds in the Met Office UKV model using observation-minus-background and observation-minus-analysis statistics. *Mon. Wea. Rev.*, **144**, 3533–3551, https://doi.org/10.1175/MWR-D-15-0340.1.

Wang, X., 2010: Incorporating ensemble covariance in the Grid-point Statistical Interpolation (GSI) variational minimization: A mathematical framework. *Mon. Wea. Rev.*, **138**, 2990–2995, https://doi.org/10.1175/2010MWR3245.1.

——, D. Parrish, D. T. Kleist, and J. Whitaker, 2013: GSI 3DVar-based ensemble–variational hybrid data assimilation for NCEP global forecast system: Single-resolution experiments. *Mon. Wea. Rev.*, **141**, 4098–4117, https://doi.org/10.1175/MWR-D-12-00141.1.

Wheatley, D. M., K. H. Knopfmeier, T. A. Jones, and G. J. Creager, 2015: Storm-scale data assimilation and ensemble forecasting with the NSSL Experimental Warn-on-Forecast System. Part I: Radar data experiments. *Wea. Forecasting*, **30**, 1795–1817, https://doi.org/10.1175/WAF-D-15-0043.1.

Wu, W.-S., R. J. Purser, and D. F. Parrish, 2002: Three-dimensional variational analysis with spatially inhomogeneous covariances. *Mon. Wea. Rev.*, **130**, 2905–2916, https://doi.org/10.1175/1520-0493(2002)130<2905:TDVAWS>2.0.CO;2.

——, D. F. Parrish, E. Rogers, and Y. Lin, 2017: Regional ensemble-variational data assimilation using global ensemble forecasts. *Wea. Forecasting*, **32**, 83–96, https://doi.org/10.1175/WAF-D-16-0045.1.

Xiao, Q., Y.-H. Kuo, J. Sun, W.-C. Lee, E. Lim, Y.-R. Guo, and D. M. Barker, 2005: Assimilation of Doppler radar observations with a regional 3DVAR system: Impact of Doppler velocities on forecasts of a heavy rainfall case. *J. Appl. Meteor.*, **44**, 768–788, https://doi.org/10.1175/JAM2248.1.